

Unclassified

2

AD-A211 489

## DOCUMENTATION PAGE

Form Approved  
OMB No. 0704-0188

1. <b>AD-A211 489</b>		1b. RESTRICTIVE MARKINGS <b>FILE COPY</b>	
2a. AUTHORITY		3. DISTRIBUTION/AVAILABILITY OF REPORT Approved for public release; distribution is unlimited.	
2b. DECLASSIFICATION/DOWNGRADING SCHEDULE		4. PERFORMING ORGANIZATION REPORT NUMBER(S)	
4. PERFORMING ORGANIZATION REPORT NUMBER(S)		5. MONITORING ORGANIZATION REPORT NUMBER(S) <b>AFOSR-TR- 89-1183</b>	
6a. NAME OF PERFORMING ORGANIZATION Penn State University	6b. OFFICE SYMBOL (If applicable)	7a. NAME OF MONITORING ORGANIZATION AFOSR/NA	
6c. ADDRESS (City, State, and ZIP Code) Mechanical Engineering Building University Park, PA 16802		7b. ADDRESS (City, State, and ZIP Code) Building 410, Bolling AFB DC 20332-6448	
8a. NAME OF FUNDING/SPONSORING ORGANIZATION AFOSR/NA	8b. OFFICE SYMBOL (If applicable) NA	9. PROCUREMENT INSTRUMENT IDENTIFICATION NUMBER AFOSR 87-0097	
8c. ADDRESS (City, State, and ZIP Code) Building 410, Bolling AFB DC 20332-6448		10. SOURCE OF FUNDING NUMBERS	
		PROGRAM ELEMENT NO. 61102F	TASK NO. 2308
		TASK NO. A2	WORK UNIT ACCESSION NO.
11. TITLE (Include Security Classification) (U) Premixed Turbulent Flame Propagation			
12. PERSONAL AUTHOR(S) D. A. Santavicca			
13a. TYPE OF REPORT Annual	13b. TIME COVERED FROM 1/1/87 TO 10/31/88	14. DATE OF REPORT (Year, Month, Day) 89, April, 10	15. PAGE COUNT
16. SUPPLEMENTARY NOTATION			
17. COSATI CODES		18. SUBJECT TERMS (Continue on reverse if necessary and identify by block number)	
FIELD	GROUP	SUB-GROUP	
19. ABSTRACT (Continue on reverse if necessary and identify by block number) <p>An experimental study has been conducted of turbulence-flame interactions in premixed turbulent flames and their effect on flame-generated turbulence, flame structure and flame propagation. The flame configuration used for this study is that of a freely propagating, one-dimensional (in the mean) turbulent flame which is free of the flame stabilization, free stream shear, and post-flame flow restriction effects of other flame configurations.</p> <p>Flame-generated turbulence has been studied in an atmospheric pressure, propane-air flame at one turbulence condition, where LDV measurements of the mean velocity, turbulence intensity, time scale, energy spectrum, length scale and Reynolds stress have been made as a function of time through the propagating flame front. A three-fold increase in the density weighted turbulent kinetic energy across the flame front is observed. Based on a comparison with similar results from other experiments, this result suggests that the heat release parameter has a greater effect on flame-generated turbulence</p> <p>(see reverse)</p>			
20. DISTRIBUTION/AVAILABILITY OF ABSTRACT <input checked="" type="checkbox"/> UNCLASSIFIED/UNLIMITED <input checked="" type="checkbox"/> SAME AS RPT. <input checked="" type="checkbox"/> DTIC USERS		21. ABSTRACT SECURITY CLASSIFICATION Unclassified	
22a. NAME OF RESPONSIBLE INDIVIDUAL Julian M Tishkoff		22b. TELEPHONE (Include Area Code) (202) 767-0465	
		22c. OFFICE SYMBOL AFOSR/NA	

DD Form 1473, JUN 86

Previous editions are obsolete.

SECURITY CLASSIFICATION OF THIS PAGE

89 8 21 093

Unclassified

19. (cont'd)

than the turbulence intensity to laminar flame speed ratio. The first direct measurements of turbulence integral length scales in a flame have been made. An increase in the length scale of approximately a factor of two across the flame front is observed, which is substantially less than what would be expected from dilatation effects. Both the turbulence intensity and length scale are found to become anisotropic in the burned gases. The energy spectrum measurements show that the turbulent kinetic energy which the flame produces is coupled into the turbulent flow at high frequencies, but that viscous dissipation in the high temperature burned gas appears to cause the energy distribution to shift toward lower frequencies. Additional measurements are being made at several different turbulence conditions in order to better understand the mechanism of flame-generated turbulence.

Measurements of the turbulent flame structure have been made using two-dimensional imaging based on Mie scattering from  $ZrO_2$  particles which are added to the flow for this purpose. These measurements have been made over a range of turbulent Reynolds numbers from 50 to 1430 and Damkohler numbers from 10 to 900 encompassing a significant portion of the reaction sheet regime of premixed turbulent combustion. The measurements have been analyzed using a fractal analysis and it has been shown that premixed turbulent flame structure is fractal over this broad range of conditions and that the fractal dimension increases monotonically with increasing turbulence intensity to laminar flame speed ratio from a laminar limit of approximately 2.05 to a high Reynolds number limit of approximately 2.35. A heuristic model has been developed which accurately predicts the observed variation in flame structure fractal dimension based on the competition between turbulence which acts to convectively distort the flame surface and burning which acts to smooth the flame surface. This heuristic fractal dimension model has been used in a fractal flame speed model which is compared to a number of other reaction sheet turbulent flame speed models. The heuristic fractal dimension model has also been used to develop a model of turbulent flame kernel growth which accounts for both the time and length scale effects of turbulence. The model has been compared with the limited turbulent flame kernel growth measurements which are available and very good agreement has been obtained between the measurements and the predictions of the fractal turbulent flame kernel model. Additional measurements, however, are required over a broad range of turbulence intensities and length scales for a more comprehensive evaluation of the model. In addition, a number of important issues regarding the fractal nature of turbulent flames require further study.

## TABLE OF CONTENTS

	<u>Page</u>
Cover Page	1
Table of Contents	2
Research Objectives	3
Status of Research	4
Description of Experiment	4
Description of Measurement Techniques	7
Flame-Generated Turbulence Measurements	9
Flame Structure Measurements	18
Turbulent Flame Kernel Growth Model	35
References	42
Publications	45
Professional Personnel	45
Interactions	45

Accession For	
NTIS GRA&I	<input checked="checked" type="checkbox"/>
DTIC TAB	<input type="checkbox"/>
Unannounced	<input type="checkbox"/>
Justification	
By	
Distribution/	
Availability Codes	
Dist	Avail and/or Special
A-1	



is not required and is  
not required by DNV-Risk 150-12.  
The following is a list of  
DNV-Risk 150-12.

## RESEARCH OBJECTIVES

The objective of this research is to develop an improved understanding of turbulence-flame interactions and their effect on turbulent flame propagation and flame generated turbulence in premixed turbulent flames. The interaction between turbulence and premixed flames can be viewed in terms of changes in the flame structure. As first proposed by Damkohler, turbulence scales which are larger than the laminar flame thickness act to convectively distort or wrinkle the flame front, thereby increasing the total flame area and, as a result, the overall mass burning rate. Turbulence scales which are smaller than the laminar flame thickness affect the overall mass burning rate as a result of increased transport rates within the flame sheet, which enhance the local laminar flame speed. The local curvature of the flame front also affects the local laminar flame speed through flame stretch effects. In addition to the effects of turbulence on flame structure, the local velocity field produced by the irregularly shaped flame front alters the turbulence properties of the flow both immediately ahead of and downstream of the flame. Although this interpretation of turbulence-flame interactions is widely accepted, there has been little experimental confirmation of its validity. The specific objective of this research is to experimentally characterize turbulence-flame interactions in premixed turbulent flames over a broad range of turbulence Reynolds and Damkohler numbers. Measurements are made of the turbulence properties both upstream and downstream of the flame, including turbulence intensity, length scale, time scale, energy spectrum and Reynolds stress, as well as of the turbulent flame structure and the turbulent burning rate. In order to quantify the role of turbulent flame structure, a fractal representation is used. These measurements provide a comprehensive characterization of turbulence-flame interactions, new insights and understanding regarding their effect on turbulent flame propagation and flame generated turbulence, and new methods for quantifying the role of turbulent flame structure in turbulent combustion models.

## STATUS OF RESEARCH

### Description of Experiment

The turbulent flow reactor used in this research, referred to as a pulsed-flame flow reactor, was specifically designed for this study of turbulence-flame interactions in premixed turbulent flames. A schematic drawing of the atmospheric pressure pulsed-flame flow reactor is shown in Figure 1. The two unique features of this flow reactor are the manner in which turbulence is generated and its pulsed or periodic operation. Turbulence is generated by forcing the fuel-air mixture through a large number (32) of small diameter (0.8mm), high Reynolds number ( $\sim 30,000$ ) jets which are uniformly distributed over the cross-section of the flow reactor and oriented normal to the axis of the flow reactor. With this device, relative turbulence intensities as high as 70% can be achieved, which are uniform within  $\pm 10\%$  over the cross-section of the flow reactor. The grid shown in Figure 1 is used to reduce the turbulence intensity and scale produced by the turbulence generator. Fuel is added to the air flow well upstream of the test section to insure complete mixing. The flame is initiated by a spark located approximately two test section diameters downstream of the measurement location. This produces a flame which freely propagates upstream through the measurement location as illustrated in Figure 1. By cycling the fuel off and on in 2 second intervals, and by adjusting the spark timing to coincide with the arrival of each fuel-air "slug", a flame is produced every 4 seconds. Measurements can then be made over many different flame events and ensemble averaged to obtain the appropriate statistical averages.

The freely propagating flame of the pulsed-flame flow reactor has several significant advantages over other flame configurations which have been used to study turbulence-flame interactions such as rod stabilized V-flames [1-5], rim stabilized conical flames [6-9], edge stabilized planar flames [10-12], and wall stabilized stagnation flames [13,14]. These advantages are:

- i. The flame is normal to the upstream flow. This is the simplest orientation and is consistent with the assumed orientation of most models;
- ii. The flow field is free of flame stabilizer effects which ensures that the local flame structure is determined solely by the turbulence;
- iii. Free stream shear in the upstream flow is negligible so that changes in turbulence through the flame must be due entirely to the flame itself; and,
- iv. The downstream flow is unrestrained so that post-flame turbulence measurements are representative of flame generated turbulence effects.

The planar flame configuration described above has been used for the flame generated turbulence measurements and the 2-D flame structure measurements. For reasons discussed later, a spherical flame configuration is used for the turbulent flame speed measurements. In this case the spark electrodes are positioned at the measurement location in order to measure the growth rate of the spherical flame kernel.

Both open and confined configurations of the atmospheric pulsed-flame flow reactor have been used as illustrated in Figure 1. The advantage of the confined configuration is that much higher turbulence intensities can be used without the problem of entrainment of the surrounding air flow. In addition, a high pressure (20 atm) pulsed-flame flow reactor has also been constructed and used in this research. A schematic drawing of the high pressure flow reactor is shown in Figure 2.

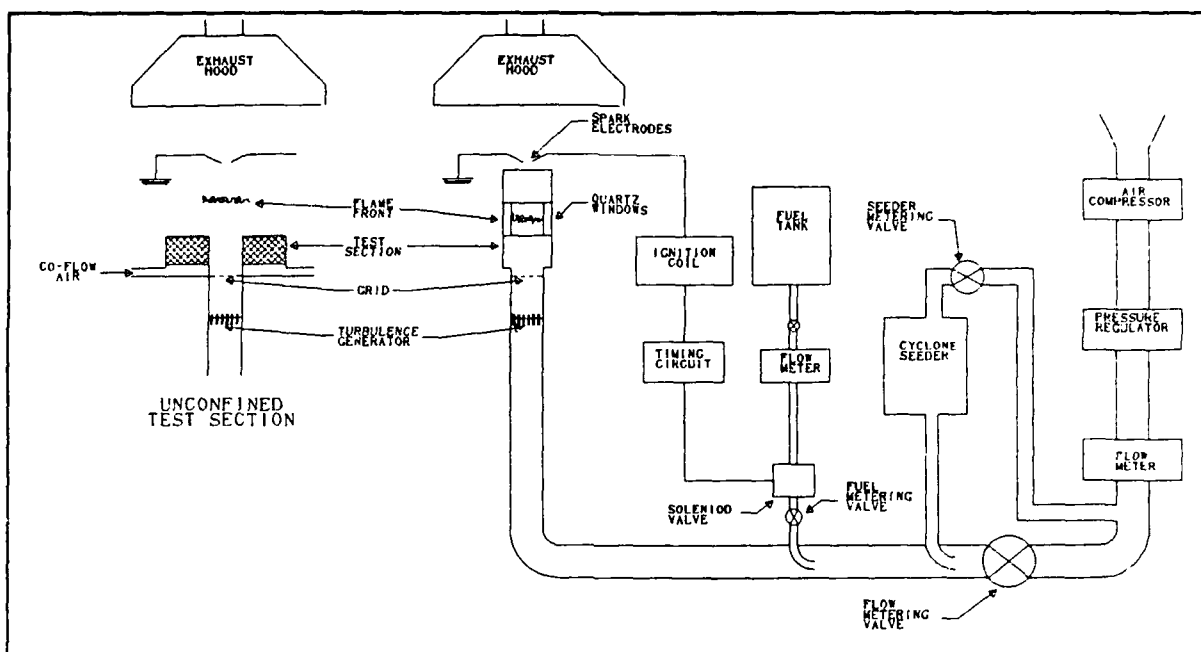


Figure 1. Schematic diagram of both confined and unconfined configurations of the atmospheric pressure pulsed-flame flow reactor.

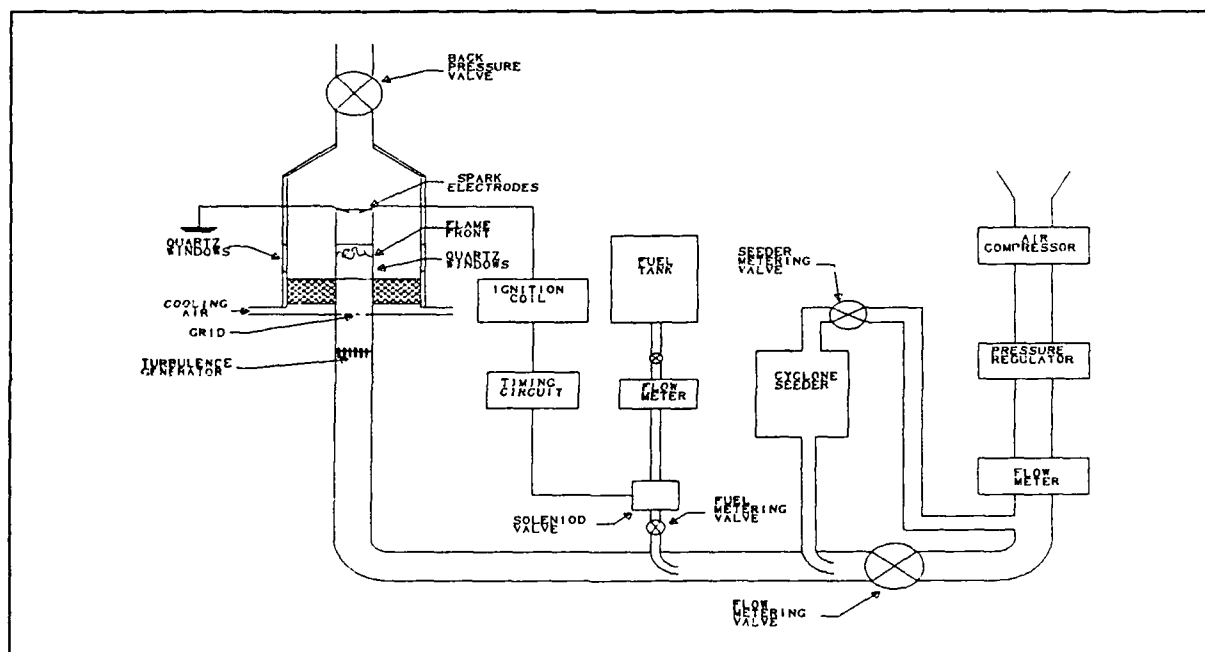


Figure 2. Schematic diagram of the high pressure pulsed-flame flow reactor.

### Description of Measurement Techniques

The three different measurement techniques which are used in this study of turbulence-flame interactions are laser Doppler velocimetry, two-dimensional imaging, and laser shadowgraphy. Each technique and the information obtained are described below.

Laser Doppler velocimetry (LDV) is used to measure the mean gas velocity and the turbulence properties in the flow reactor under cold flow conditions and as a function of time through the propagating flame front. The LDV system is an argon ion based two-color system which can be configured to make simultaneous measurements of two velocity components at the same spatial location or the same velocity component at two different spatial locations. Measurements are made of the mean velocity, turbulence intensity, energy spectrum, time scale, length scale and Reynolds stress. Velocity components and length scales are measured in directions both parallel and perpendicular to the mean flame front. The length scale is obtained directly from a two-point spatial correlation measurement. A 20 microsecond coincidence window is used for the two-point and the Reynolds stress measurements.

The turbulence properties calculated from the cold flow velocity measurements are obtained using a time averaged analysis, whereas an ensemble averaged analysis is used to calculate the turbulence properties from the velocity measurements made through the propagating flame front. In the ensemble averaged analysis, the velocity-time records from individual flame events are shifted to match flame arrival times before the data is processed. Two methods for determining flame arrival have been used. One method is based on the sudden increase in velocity which occurs across the flame front. This method, however, only works if the measured velocity component is normal to the local flame front. A second, more reliable, method is to use a separate photomultiplier tube to collect light scattered by the seed particles in the LDV probe volume. The photomultiplier signal is low-pass filtered to eliminate the high frequency Doppler component. Flame arrival at the LDV probe volume is clearly indicated by a marked decrease in the scattered light intensity due to both the decreased particle density and particle deagglomeration which occurs in the post-flame gases. The flame arrival signal is also used to selectively inhibit the LDV counter processor so as to only take measurements in either the unburned or burned gases. This makes it possible to independently optimize the LDV system for measurements in either the burned or unburned gases which has significantly increased the data rate which can be obtained in the burned gases. This is important for successful length scale and Reynolds stress measurements in the burned gases since it partially compensates for the approximate factor of ten reduction in data rate when coincident measurements are made.

Two-dimensional imaging is used to measure the flame structure. This technique involves focusing the frequency doubled output of a pulsed Nd:YAG laser to form a 5cm high by 500 micron wide laser sheet which passes through the flame front, as illustrated in Figure 3. The 10 nsec laser pulse is synchronized with the passage of the flame front, as indicated by the refraction of a helium-neon laser beam off a small photodiode detector. The air flow is seeded with nominal 1 micron zirconium oxide particles, and the light scattered from the laser sheet by the particles is



imaged onto a 128x128 diode array camera. The camera output is recorded using a PC-based video frame grabber. Depending on the equivalence ratio, there is a 5-8 fold decrease in particle density across the flame front. In addition, there is significant particle deagglomeration. These two factors result in an order of magnitude difference in the scattered light intensity from the unburned to burned gas regions of the two-dimensional image detected by the camera. Using background subtraction, thresholding and filtering techniques, the image is converted into two colors, which represent the burned and unburned regions of the flame. The interface corresponds to the two-dimensional flame structure defined by the intersection of the flame front and the laser sheet. A 4cm by 4cm field of view is used resulting in a 300 micron pixel resolution.

Laser shadowgraphy is used to measure the turbulent flame speed. The output of an argon ion laser is passed through a spatial filter, beam expander and aperture to form a 60mm diameter beam of uniform intensity which is passed through the flame front to produce a shadowgraph image which is recorded on a Spin-Physics camera at 2000 frames per second. As noted previously, the flame configuration used for the flame speed measurement is that of a spherical flame kernel produced by moving the ignition location upstream to the measurement location. The boundary of the flame kernel image is manually digitized, from which the projected area of the flame kernel is determined. This area is then used to calculate an "equivalent radius" of a perfectly spherical flame kernel. The result is in the form of the equivalent flame kernel radius as a function of time following ignition.

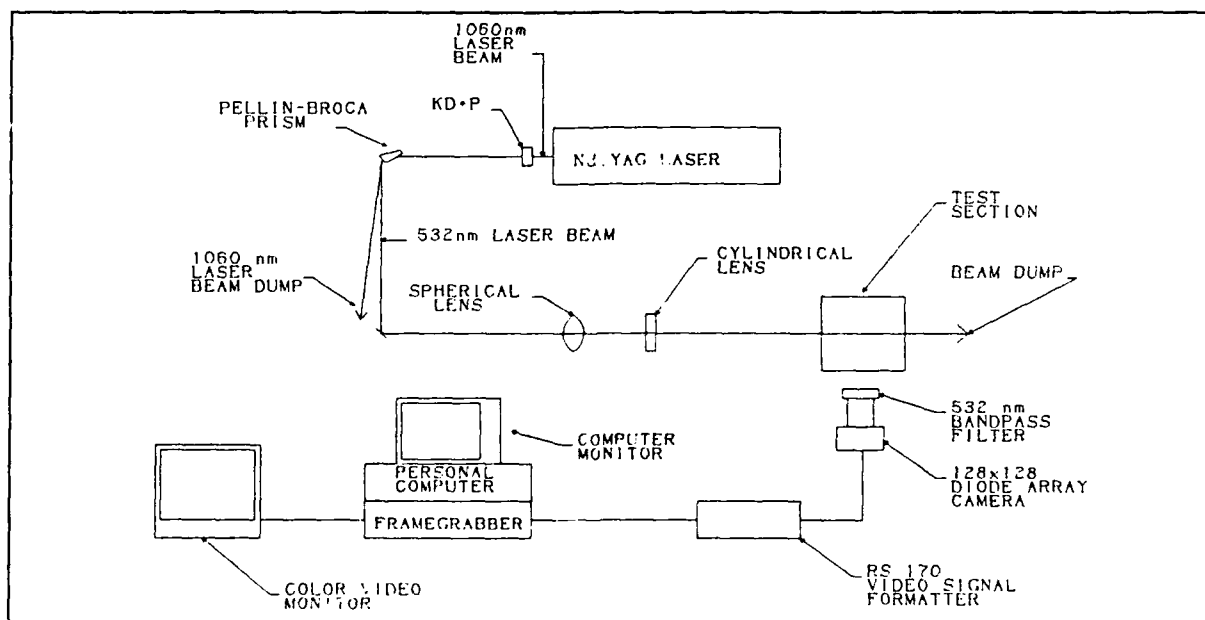


Figure 3. Schematic diagram of the two-dimensional flame structure measurement apparatus.

### Flame-Generated Turbulence Measurements

The effect of turbulence-flame interactions on the turbulence properties of the flow both upstream and downstream of the flame front has been extensively studied in a propane-air flame at an equivalence ratio of 1.0, a pressure of 1 atmosphere, a temperature of 300 K, a turbulence intensity of 25 cm/sec and an integral length scale of 8.2 mm. The LDV system described in the previous section has been used to measure the mean velocity, turbulence intensity, time scale, energy spectrum, length scale and Reynolds stress as a function of time through the propagating flame front. Velocity components and length scales are measured both normal and parallel to the mean flame front. The velocity measurements are made on the centerline of the flow reactor in the unconfined configuration shown in Figure 1.

In discussing the results of this study, reference will be made to a number of other studies of turbulence-flame interactions. The operating conditions and results of these studies, as well as the present study, are summarized in Table 1.

The mean velocity, both normal and parallel to the flame front, is plotted in Figure 4 as a function of time through the propagating flame, where flame arrival occurs at  $t=0$ . The mean velocity component parallel to the mean flame front shows no appreciable change across the flame, whereas the normal component shows a gradual decrease immediately ahead of the flame and a sudden, large increase across the flame. The observed decrease in the mean velocity ahead of the flame is due to the unconfined nature of the flame and reflects the fact that some of the unburned gas ahead of the flame is actually diverted around the flame. The sudden increase across the flame is due to the flame's chemical heat release and the resultant thermal expansion. Again, however, there is evidence of the unconfined nature of this flame in that the velocity increase is approximately half of what would be expected for a one-dimensional thermal expansion.

The turbulence intensity, measured both normal and parallel to the mean flame front, is shown in Figure 5, where again flame arrival occurs at  $t=0$ . The turbulence intensity normal to the mean flame front is observed to gradually increase by approximately 50% ahead of the flame and then to suddenly increase by a factor of 5 to 6 across the flame. Whereas the turbulence intensity parallel to the mean flame front shows no appreciable increase ahead of the flame and only a factor of 2 to 3 increase across the flame. Since there is a significant decrease in density across the flame, it is more appropriate to consider the density weighted turbulent kinetic energy,  $\rho u'^2$ , which is plotted in Figure 6 and shows that there is a nearly three-fold increase in turbulent kinetic energy across the flame as a result of the turbulence-flame interactions. It is also important to note that the turbulence production is highly anisotropic and that any model of turbulence-flame interactions must not only account for the turbulence production but its anisotropic nature as well.

Both the turbulence intensity to the laminar flame speed ratio [15] and the heat release parameter [16] have been suggested as important parameters for characterizing flame generated turbulence. However, this can not be resolved with the present measurements which are at a single operating condition. Other measurements of the effect of turbulence-flame interactions on the post-flame turbulence intensity have been reported, as summarized in Table 1. However, the results are

Table 1. Summary of experimental studies of turbulence-flame interactions in premixed flames.

Authors (Date)	Flame Configuration	Upstream Intensity (cm/sec)	Upstream Integral Scale (mm)	Heat Release Parameter ( $T_b/T_u - 1$ )	Coordinate System	Conditioning Technique
Bill et al. [1]	V-flame	10-30		5.1-6.0	Axis (u) and radius (v) of burner exit	None
Dandekar, Gouldin [2]	V-flame	30	1.9	5.4-6.4	Same	None
Cheng, Ng [3]	V-flame	23-66	5.0	5.4-5.7	Same	None
Cheng [4]	V-flame	27		5.7	Same	Based on seeding: oil droplets in reactants, $AlO_2$ through the flame
Gokalp et al. [5]	V-flame	30,49	5.7,3.0	6.0,6.2		
Yoshida, Tsuji [6]	Conical (D=10mm)	18		5.4	Axis (u) and radius (v) of burner exit	None
Yoshida [7]	Conical (D=40mm)	32		5.7	Same	None
Shepherd, Moss [8]	Conical (D=50mm)	30		5.4	Same	Mie scattering intensity
Cheng, Shepherd [9]	Conical (D=50mm)	66	16.5	5.1	Same	Based on seeding: oil droplets in reactants, $AlO_2$ through the flame
Gulati, Driscoll [10,11,12]	Oblique, planar	12	1.0	5.0, 5.5, 6.4	Normal (u) and tangent (v) to flame front	Rayleigh scattering
Cho et al. [13,14]	Stagnation stabilized	30, 45	2.0	5.0, 5.5, 6.4	Normal (u) and tangent (v) to flame front	Based on seeding: oil droplets in reactants, $AlO_2$ through the flame
Videto, Santavicca (Present)	Freely propagating	25	8.0	6.6	Normal (u) and tangent (v) to flame front	Mie scattering intensity

Table 1. (Continued)

Authors (Date)	Turbulence Intensity $u'$	Turbulence Intensity $v'$	Integral Length Scale	Integral Time Scale	Energy Spectrum
Bill et al. [1]	Radial profile: decreased overall by 50%*				
Dandekar, Gouldin [2]	Radial profile: decreased overall by 50%*	Radial profile: decreased overall by 30%*			
Cheng, Ng [3]	Radial profile: No change overall*	Radial profile: No change overall*	Tripled across flame (based on Taylor's hypothesis)		
Cheng [4]	Radial profile: $u'$ not effected, $u'$ twice $u'$ in flame but decays in products	Radial profile: Trends same as for $u'$ , although $v'_p$ was 20% lower than $v'_r$			
Gokalp et al. [5]	Same data as in Cheng, Ng (1983)		Roughly doubled (based on Taylor's hypothesis)	Trend dependent on incident turbulence	Energy shifted toward larger scales in product region
Yoshida, Tsuji [6]	Axial profile: Decreased 25%, but increased near tip Radial profile: Increased 25%				
Yoshida [7]	Radial profile: Nearly doubled	Identical to $u'$ throughout flame			
Shepherd, Moss [8]	Axial profile: $u'$ doubled, $u'_p$ slightly larger				
Cheng, Shepherd [9]	Radial profile: $u'_r$ , $u'_p$ constant, Axial profile: $u'$ decreased 25% $u'_p$ constant	Radial profile: $v'_r$ , $v'_p$ decreased 50% Axial profile: $v'_r$ decreased 35% $v'_p$ increased 15%			
Gulati, Driscoll [10,11,12]	Normal profile: $u'_r$ and $u'_p$ several times larger than upstream level, $u'_p$ constant downstream	Normal profile: doubled overall			
Cho et al. [13,14]	Normal profile: $u'_r$ and $u'_p$ equal and unchanged in flame, but $u'$ decayed downstream	Normal profile: $v'_r$ not changed by flame, $v'_p$ 50% higher than $v'_r$ both in and behind the flame			
Videto, Santavicca (Present)	Normal profile: $u'_r$ increased by 50% ahead of flame, $u'_p$ 5 to 6 times the upstream level	Normal profile: $v'_r$ unchanged ahead of the flame, $v'_p$ twice the upstream level	Normal profile: $L_\perp$ doubled, $L_\parallel$ increased 50%	Non-steady ahead and behind flame	Increased energy of high frequencies ahead of the flame, but energy energy shifted to larger scales in products

\* apparent increase in reaction zone is dominated by intermittency and therefore is not included.

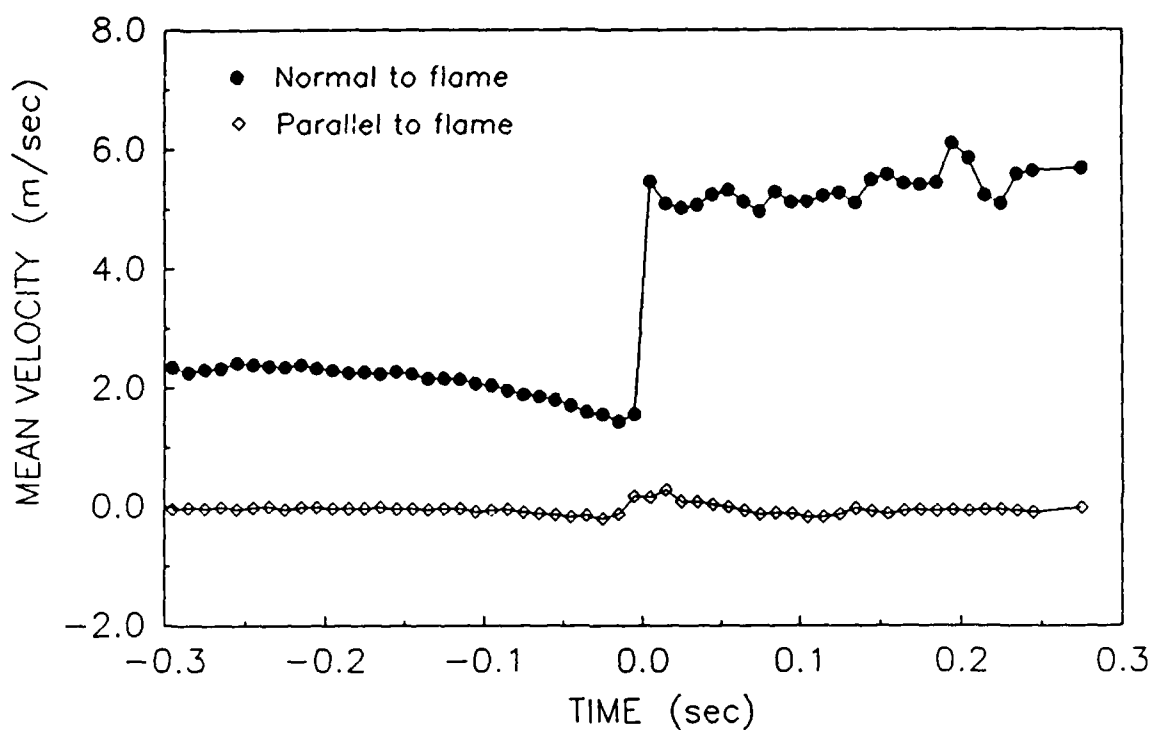


Figure 4. Normal and parallel mean velocities as a function of time. Flame arrival corresponds to  $t = 0$ .

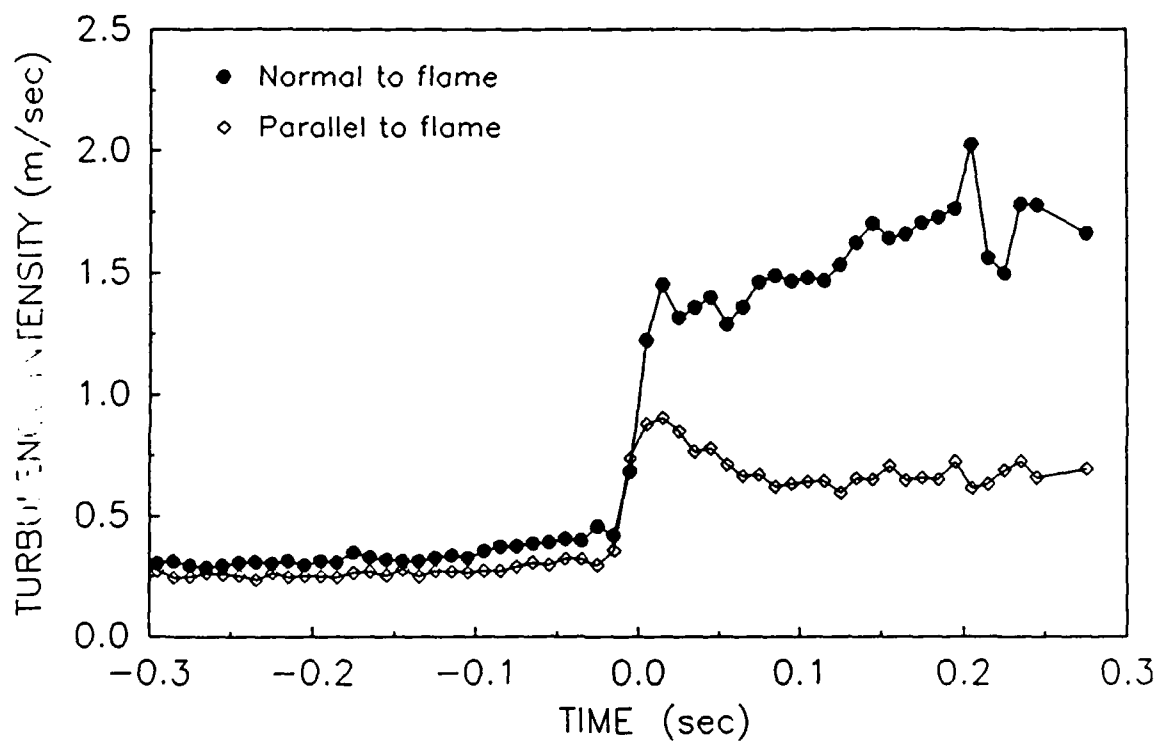


Figure 5. Normal and parallel turbulence intensities as a function of time.

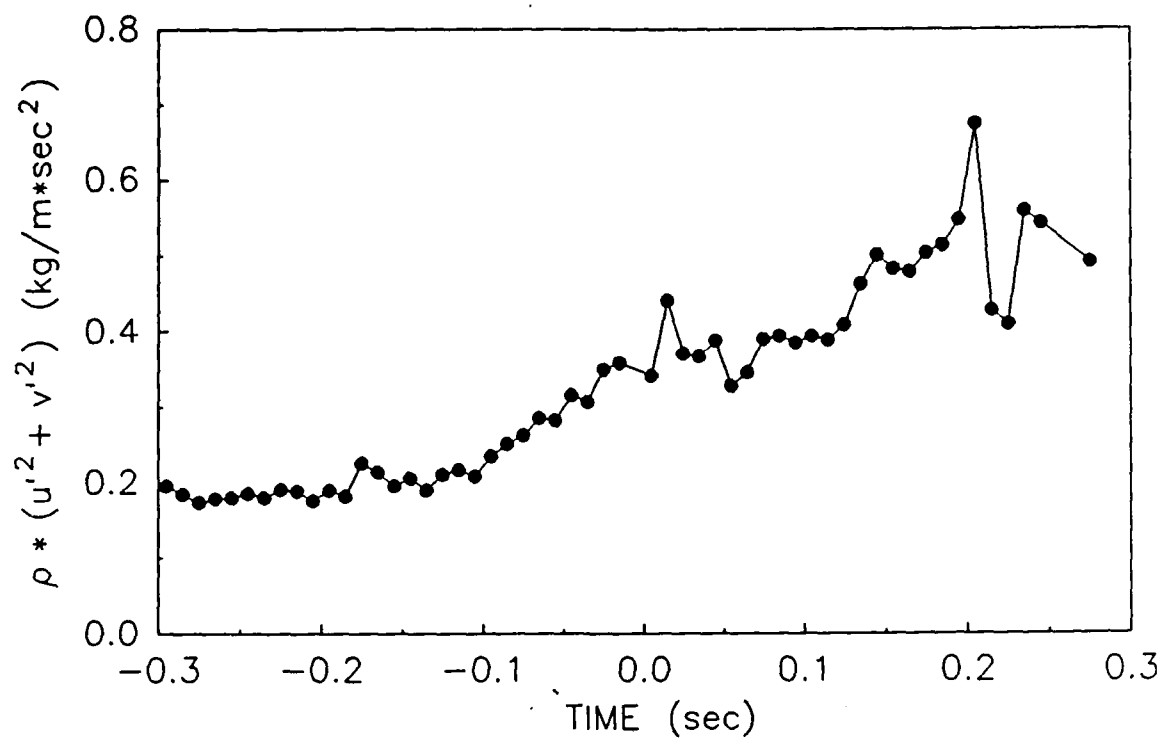


Figure 6. Density-weighted total kinetic energy as a function of time.

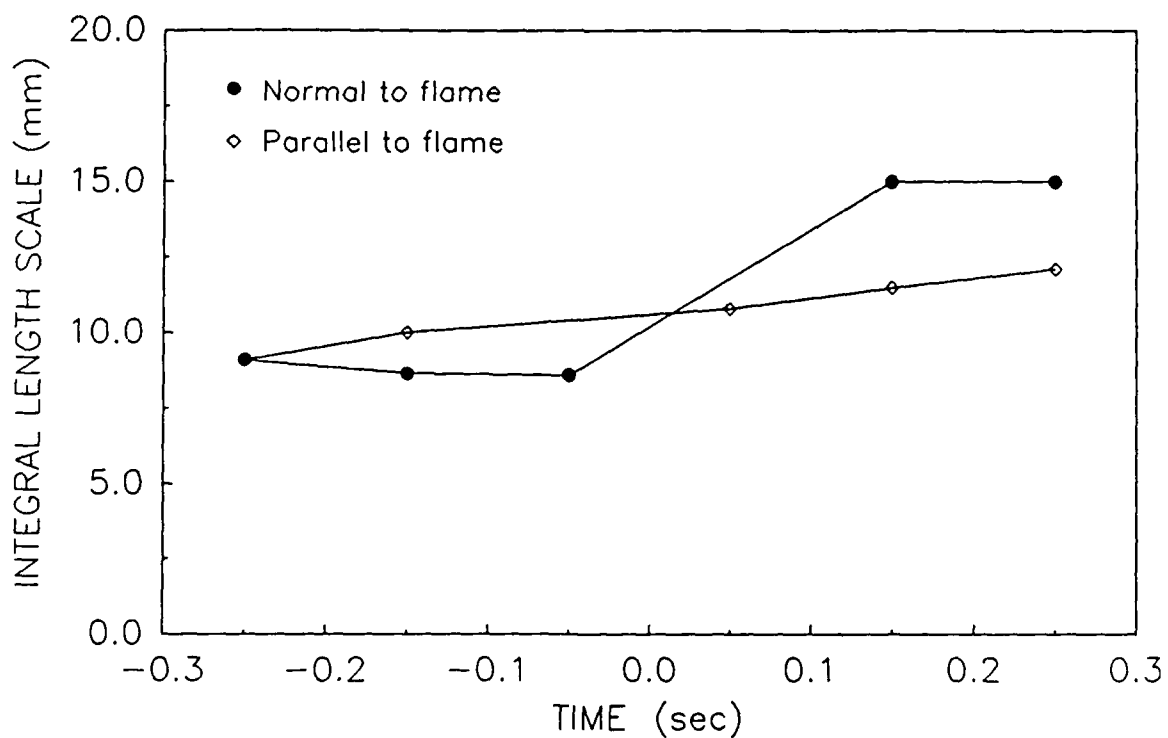


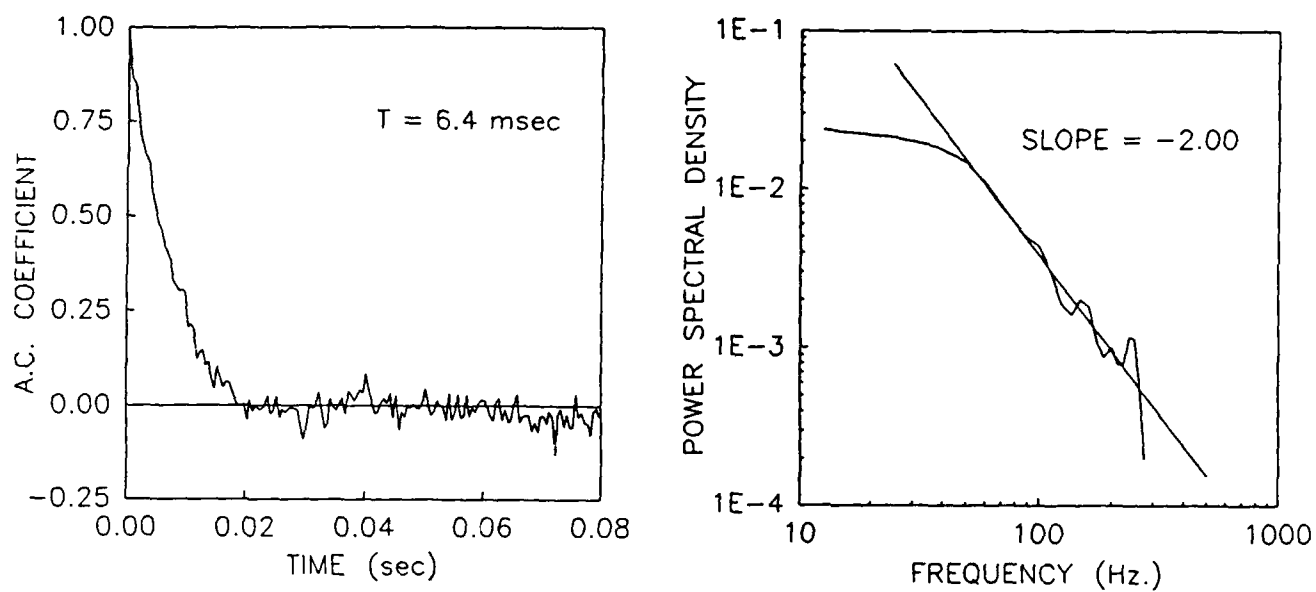
Figure 7. Normal and parallel turbulence integral length scales as a function of time.

very inconsistent and therefore difficult to interpret. A number of studies report a decrease [1,2,4,6,9] or no change [3,13,14] in the turbulence intensity across the flame zone. The flame configurations used in these studies, however, are subject to the effects of flame stabilization, free stream shear and post-flame flow restriction discussed previously and therefore are of questionable value. Results from an edge-stabilized flame configuration [10,11] which was designed to avoid the effects of free stream shear and post-flame flow restriction, however, do agree with the present results in that for the same value of the heat release parameter both studies report an approximately 5-fold increase in the turbulence intensity normal to the mean flame front. Since the upstream turbulence intensity differed by a factor of two between the two studies, this comparison suggests that the heat release parameter has a more significant effect on flame-generated turbulence. Obviously more measurements are needed to address this important question. Such measurements will be made in the pulsed-flame flow reactor over a range of turbulence intensities and heat release parameter conditions in the near future.

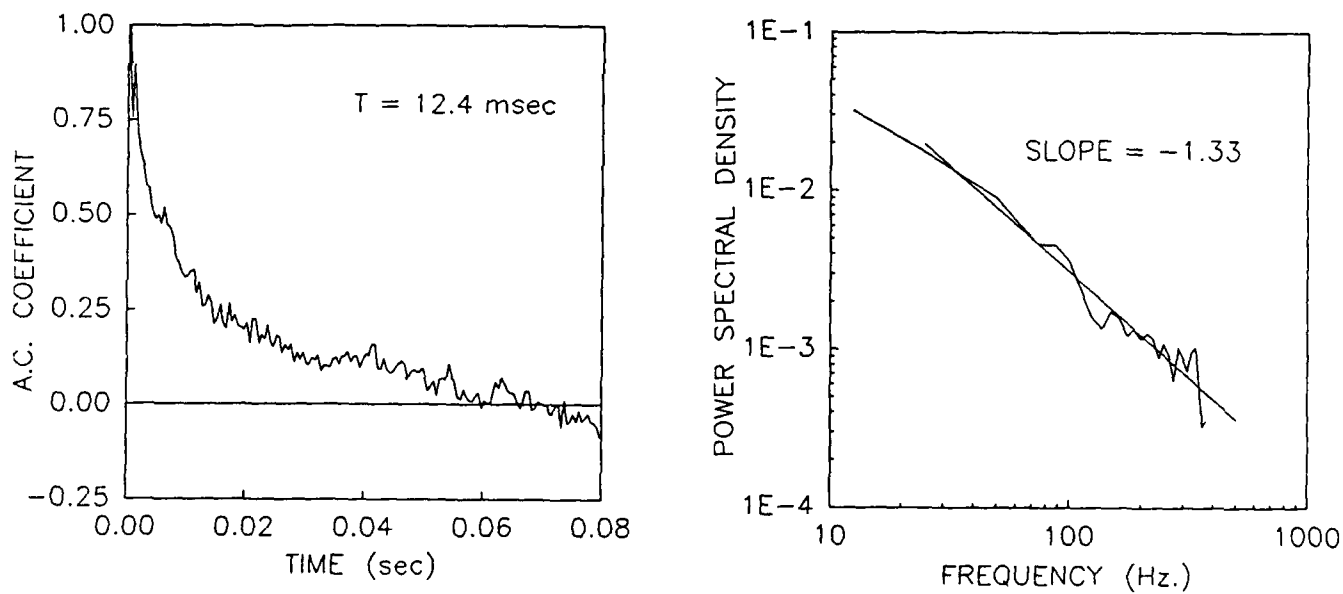
The integral length scale measurements are shown in Figure 7, where again they are plotted as a function of time and flame arrival corresponds to  $t=0$ . The length scale which is measured is a transverse length scale, using a direct two-point spatial correlation measurement. Length scales both normal and parallel to the mean flame front have been measured. The results show that the length scale increases from the unburned to the burned gases, increasing by 50% for the length scale which is parallel to the mean flame front and by a factor of 2 for the length scale which is normal to the mean flame front. The length scale measurements also reflect the fact that the upstream turbulence is relatively isotropic, but becomes anisotropic in the post-flame gases.

One reason for the change in length scale from the unburned to the burned gas is simply due to dilatation whereby one would expect the length scale to increase in proportion to the increase in the gas temperature. These results, however, do not support the idea that dilatation is the only mechanism affecting the length scale. It is also possible that turbulence production by the flame occurs predominately at scales smaller than the expected burned gas length scale. The flame structure measurements which are presented in the following section support this idea in that the largest scales in the flame structure are comparable to the upstream gas integral length scale. Again, additional measurements are needed and planned to further clarify this issue. It should be noted that these measurements of the turbulence integral length scale are the only direct length scale measurements which have been made in the unburned and burned gases of a premixed turbulent flame. A few measurements have been reported in a V-flame configuration which were obtained from a time scale measurement using Taylor's hypothesis [3,5]. Although these measurements are consistent with the results of this study, the validity of Taylor's hypothesis in the burned gases is questionable. For example, use of the time scale measurements discussed below and Taylor's hypothesis gives a burned gas length scale which is a factor of 2 greater than the directly measured length scale in this study.

The integral time scale and the turbulence energy spectrum results ahead of and behind the flame are shown in Figures 8 and 9, respectively. Also shown are the temporal autocorrelation



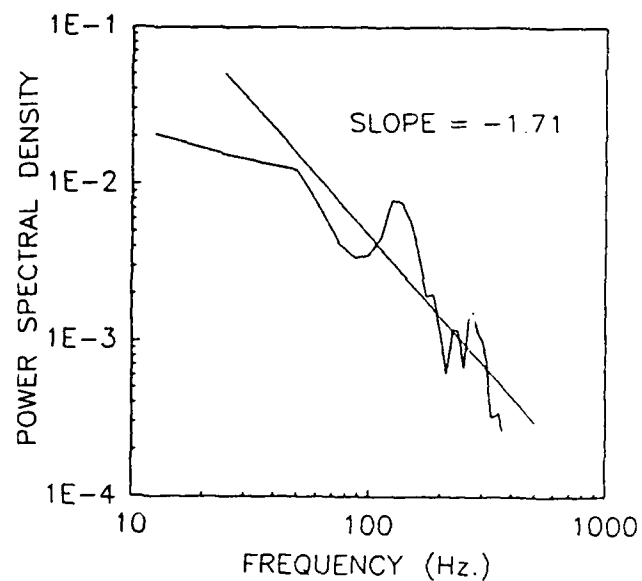
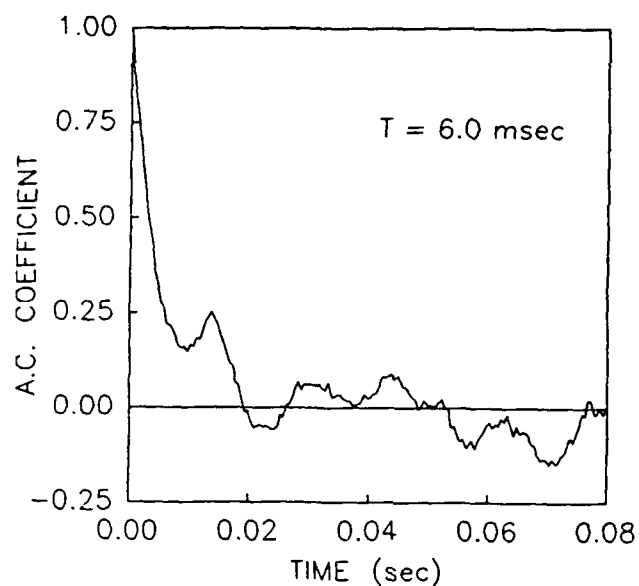
(a) 225 msec. before flame arrival.



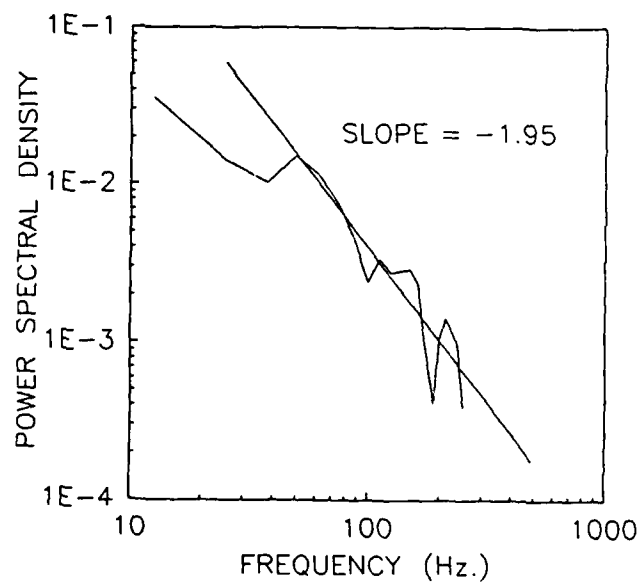
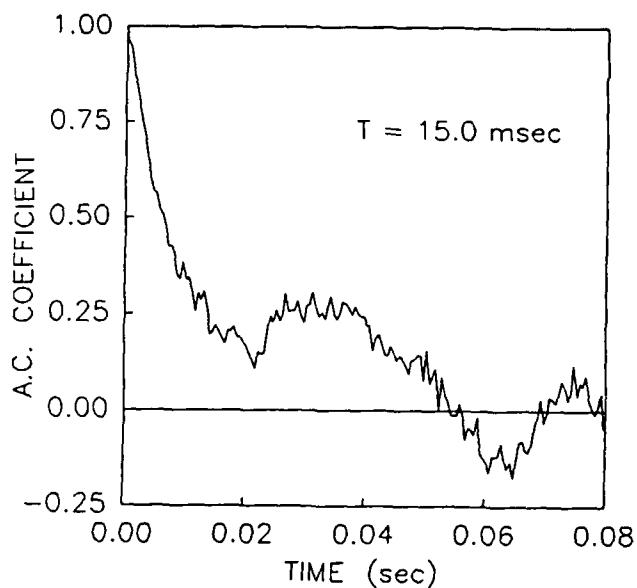
(b) 75 msec. before flame arrival.

Figure 8. Autocorrelation and turbulence energy spectrum curves ahead of the flame.





(a) 75 msec. after flame arrival.



(b) 225 msec. after flame arrival.

Figure 9. Autocorrelation and turbulence energy spectrum curves behind the flame.

curves from which both the integral time scales and the energy spectra are calculated.

Measurements are shown for 225 msec and 75 msec before flame arrival, as well as 75 msec and 225 msec after flame arrival. Each measurement corresponds to an average over a 150 msec interval centered on each of the indicated times. The energy spectrum at 225 msec ahead of the flame shows a slope of  $-2.0$  which indicates that the turbulence is not fully equilibrated. This is actually before the flame is ignited and therefore is a measure of the cold flow turbulence. At 75 msec before flame arrival there is a pronounced increase in the high frequency content of the energy spectrum resulting in a slope of  $-1.33$ . As shown in Figure 5, there is also a noticeable increase in the turbulence intensity component normal to the flame front at this time. These results indicate that the turbulence-flame interactions, which result in an increase in the turbulent kinetic energy of the unburned gas immediately ahead of the flame, occur selectively at high frequencies and small scales of the turbulence energy spectrum. In the burned gases behind the flame a decrease in the high frequency content of the energy spectrum is observed resulting in a slope of  $-1.71$  at 75 msec and  $-1.95$  at 225 msec. To date, there has been only one other study of the effect of turbulence-flame interactions on the turbulence energy spectrum [5]. The results of this study show similar behavior in the burned gas energy spectrum. As suggested in this study, this may be due to the increased viscosity in the high temperature burned gases and its dissipative effect on the small scale eddies. Additional measurements of the effect of turbulence-flame interactions on the turbulence energy spectrum are essential. Such measurements will identify the scales on which turbulence-flame interactions take place and thereby improve our understanding of the underlying fluid mechanical mechanisms.

### **Flame Structure Measurements**

Two-dimensional flame structure measurements in turbulent propane-air flames have been made over a range of Reynolds numbers from 50 to 1430 and Damkohler numbers from 10 to 900. This also corresponds to a range of turbulence intensity to laminar flame speed ratios from 0.25 to 12. The experimental conditions are summarized in Table 2. Turbulent premixed combustion is typically separated into combustion regimes as illustrated in Figure 10. The operating conditions used in this study are also shown in Figure 10, where it is seen that except for one case, all of the flame structure measurements are in what is referred to as the reaction sheet regime.

Flame structure images at each of three different values of  $u'/S_L$  which span the range of conditions used in this study are shown in Figure 11. The field of view in each image is 4 cm by 4 cm, corresponding to a 300 micron pixel resolution. The flame is propagating downward, with the burned gas cross-hatched, the unburned gas white and the flame front defined by the interface. At each of the operating conditions listed in Table 2, between 15 and 35 images were recorded. Two important observations can be made from these images regarding the effect of increasing  $u'/S_L$ . One is that there is more evidence of small scale flame structure, and the second is that the flame zone covers a larger portion of the field of view, i.e. it becomes more space-filling, as  $u'/S_L$  increases. These observations are consistent with the fractal analysis of the flame structure images which is used to quantitatively characterize the observed changes in flame structure. Before presenting the results of this analysis, it is necessary to review the basic concepts of fractal geometry and their application to turbulent flows and turbulent flames.

Fractal theory provides a method of characterizing geometries which can not be described by conventional methods of Euclidean geometry. This area of mathematics was largely conceived and popularized by Mandelbrot [17]. The theory of fractals is particularly useful in characterizing naturally occurring geometries which do not display an abundance of normal Euclidean shapes, but exhibit a wide range of self-similar shapes and forms. This self-similar nature is characteristic of many physical forms such as trees, clouds, and mountains, and is a fundamental characteristic of fractal geometry. The self-similar nature of such shapes is characterized by the fractal dimension.

An important practical consequence of the self-similar nature of fractal objects is that the measured size of the object varies with the measurement scale by a power law. For example, the measured length,  $L$ , of a fractal curve varies with the length of scale,  $\epsilon$ , used to measure it by,

$$L \propto \epsilon^{1-D} \quad (1)$$

where  $D$  is the fractal dimension. The power law scaling of fractals, therefore, provides a method of determining the fractal dimension of a fractal object for both geometric and natural fractals. Consider the case of a fractal curve. The total length of the curve,  $L$ , can be calculated for each measurement scale,  $\epsilon$ , and plotted on a  $\log(L)$  vs.  $\log(\epsilon)$  scale as shown in Figure 12. Since the curve is fractal, a straight line is obtained with a slope of  $1-D$ , where  $D$  is the fractal dimension. The increase in length with decreasing measurement scale can be understood by noting that with

Table 2. Experimental Conditions for 2-D flame structure measurements.

$u'$ [m/s]	$\phi$	$u'/S_L$	Re	Da	$\delta_L$ [ $\mu\text{m}$ ]	$\omega_k$ [ $\mu\text{m}$ ]	$D_f$	$\sigma_D$
0.10	1.0	0.24	52	889	37.3	570	2.13	0.013
0.14	1.0	0.33	73	668	37.3	435	2.14	0.021
0.16	1.0	0.37	84	592	37.3	400	2.14	0.021
0.21	1.0	0.51	107	435	37.3	320	2.13	0.012
0.25	1.0	0.60	128	370	37.3	280	2.17	0.030
0.25	0.9	0.61	128	351	38.2	280	2.17	0.030
0.25	0.8	0.65	128	310	40.7	280	2.18	0.027
0.25	0.76	0.68	128	276	43.8	280	2.15	0.042
0.42	1.0	0.99	218	222	37.3	140	2.19	0.054
0.42	0.65	1.47	218	101	55.0	140	2.20	0.054
1.08	1.0	2.57	564	85	37.3	70	2.26	0.065
1.08	0.7	3.39	564	49	49.2	70	2.26	0.075
1.08	0.6	4.80	564	24	69.7	70	2.29	0.063
2.73	1.0	6.51	1431	34	37.3	34	2.25	0.075
2.73	0.6	11.9	1431	10	68.2	34	2.32	0.056

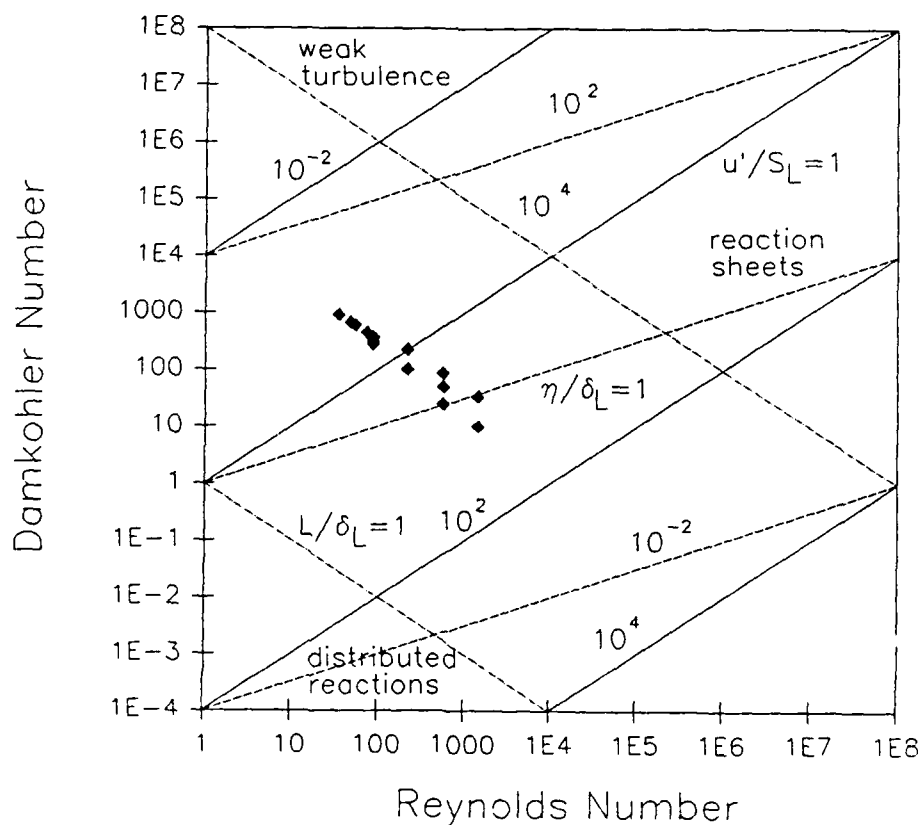


Figure 10. Damkohler vs. Reynolds number plot of the experimental conditions.

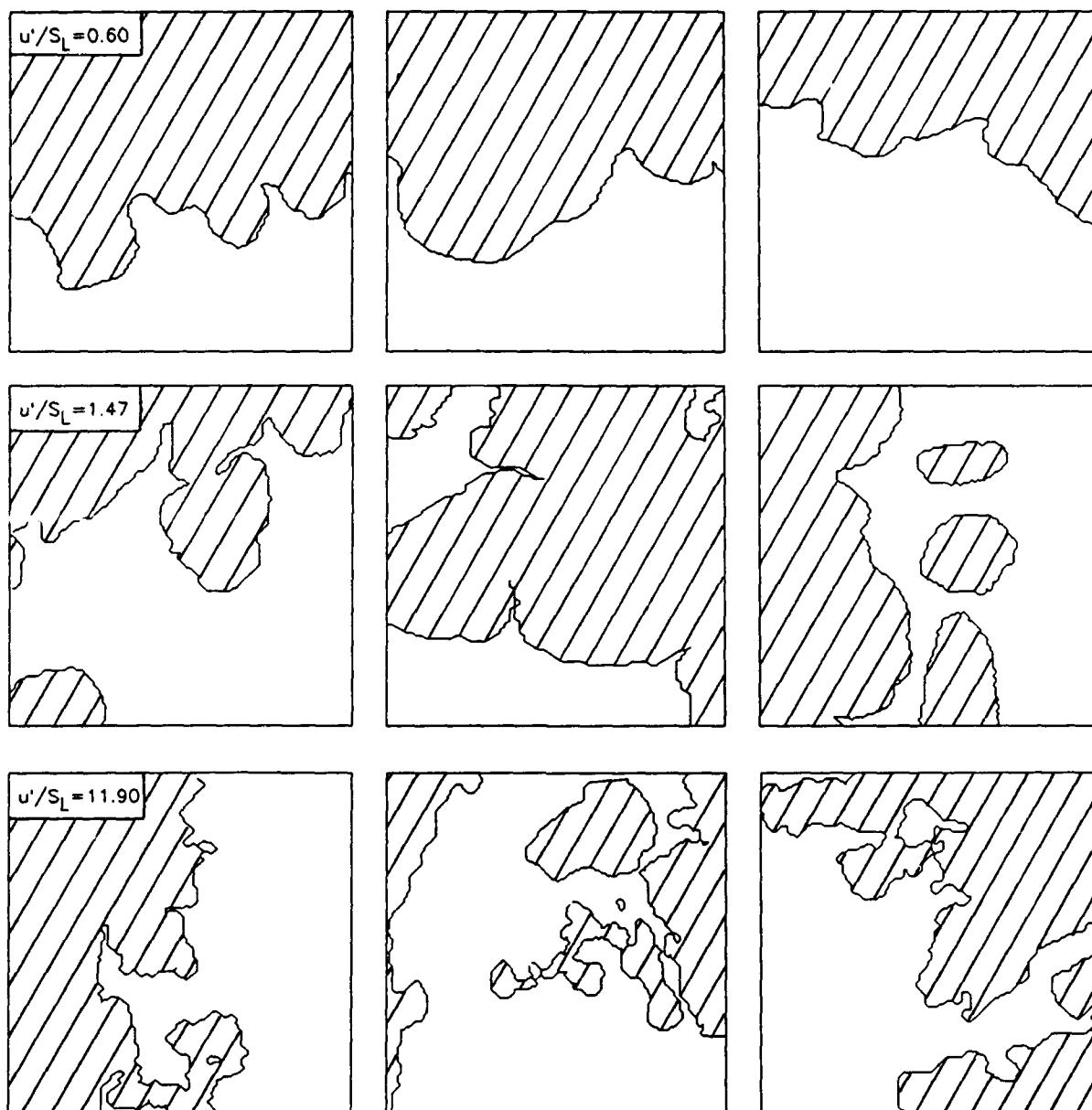


Figure 11. Typical flame structure images at three different flow conditions.

each finer measurement scale, smaller structures are resolved which add to the length of the curve.

For the case of natural fractal geometries, it is reasonable to expect there to be a minimum and maximum scale beyond which the measured size does not change. These small and large limits to the fractal behavior are referred to as the inner ( $\epsilon_i$ ) and outer ( $\epsilon_o$ ) cutoffs, respectively, and are illustrated in Figure 12.

The above concepts apply to fractal dusts, curves and surfaces, where fractal dusts are a series of points which display fractal character and exhibit fractal dimensions between 0 and 1, fractal curves exhibit fractal dimensions between 1 and 2 as already discussed, and fractal surfaces are extensions of the ideas of fractal curves into three dimensions and exhibit fractal dimensions between 2 and 3. A useful feature of isotropic fractal surfaces is that the fractal dimension of a curve defined by the intersection of a plane with the surface is simply one less than that of the fractal surface. This fact will be used when analyzing the measurements obtained in this study.

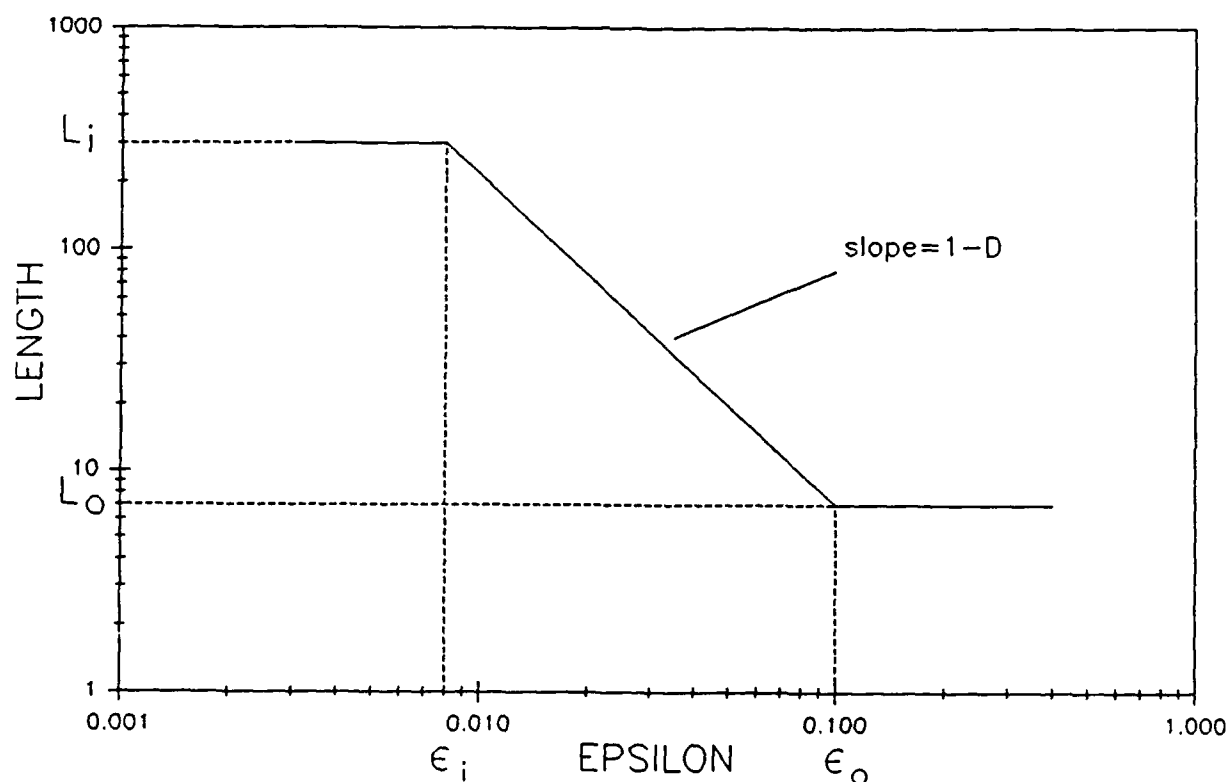


Figure 12. Theoretical fractal behavior with inner and outer cutoffs.

The hierarchy of scales present in turbulent flows is a natural subject for the application of fractal concepts, and in fact turbulent flows do exhibit fractal character as discussed below. In the case of turbulent flames it can be argued that at high Reynolds numbers, where the flame structure is dominated by the effects of turbulence, that the flame surface behaves as a passive scalar surface and that its structure is solely a function of the turbulence. Therefore, an understanding of the fractal nature of turbulence is essential to understanding the fractal nature of turbulent flames.

Most fractal theories of turbulence are related to energy cascade arguments, such as that of Kolmogorov [18], which contend that the turbulent flow consists of a series of self-similar scales governed by energy addition in the large scales which cascades through the inertial subrange and dissipates into heat through viscosity at the small scales. Based upon dimensional arguments, it can be shown that the energy spectrum of turbulent flow undergoing this process should decay with a characteristic  $5/3$  exponent in the inertial subrange. Within this energy cascade, it is possible to define surfaces of constant velocity, which are convected within the turbulent flow field. Mandelbrot [19] has shown that one can apply fractal theory to these isovelocity surfaces to obtain a characteristic fractal dimension for a given velocity distribution. Assuming a Gaussian velocity distribution, Mandelbrot derives an isovelocity surface fractal dimension of 2.67. In fact, it can be shown that for a Gaussian distribution, the fractal dimension of isovelocity surfaces can be obtained directly from the energy spectrum using the relationship,

$$D = E + (3-A)/2 \quad (2)$$

where  $E$  is the Euclidean dimension, in this case 2, and  $A$  is the slope of energy spectrum [20]. The isovelocity surface fractal dimension has been argued to equal the fractal dimension of passive scalar surfaces, such as surfaces of constant temperature or composition, however as discussed below this is incorrect.

A direct calculation of the fractal dimension of passive scalar surfaces has been recently carried out. Instead of assuming that the fractal dimension of the passive scalar surface is equal to the isovelocity fractal, Hentschel and Procaccia [21,22] have argued that passive scalar surfaces are dominated by the process of relative turbulent diffusion between particles. Single particle diffusion is dominated by the action of the large scale eddies, however, particle pairs are governed by a different scaling relationship which is dominated by eddies the size of the interparticle distance. This leads to a fractal dimension of the passive scalar surface which differs from but is related to the fractal dimension of the isovelocity surface. Arguing that the fractal dimension of the turbulent velocity field is between 2.5 and 2.67, one obtains, according to the relative turbulent diffusion model, a passive scalar fractal dimension between 2.37 and 2.41.

Experimental confirmation of this result has been obtained by several investigators. The first experimental evidence of the fractal nature of passive scalars in turbulent flows was obtained by Lovejoy [23] from the area-perimeter relationship of clouds in satellite photographs. The fractal dimension can be calculated from the area-perimeter relationship using the relationship  $P \propto (A^D)^{1/2}$ .

Since clouds exist in atmospheric turbulence, one would expect these structures to display the fractal character of turbulent structures discussed above. Satellite photos resolving scales between 1 and 1000 kilometers were studied and both the perimeter and area calculated. A least squares fit of the data produced an estimate of 2.35 for the fractal dimension of cloud surfaces with a correlation of 0.994. Note that this value agrees well with the passive scalar fractal dimension derived from the relative turbulent diffusion model.

In another experimental study, Sreenivasan [24] applied the concepts of fractal geometry to a study of turbulent/non-turbulent flow interfaces in turbulent boundary layers, axisymmetric jets, and several other flows. Two-dimensional images of the interface were obtained by seeding the turbulent flow with smoke and passing a laser sheet through the flow to produce a two-dimensional image of the instantaneous turbulent mixing layer. As discussed previously, the fractal dimension of the intersection of a plane and a fractal surface is equal to one less than the surface fractal dimension. At high turbulence levels, the images did not necessarily contain one continuous boundary, but a complex series of islands, similar to the two-dimensional flame structure images under highly turbulent conditions obtained in this study. The fractal dimensions obtained by Sreenivasan were between 2.3 and 2.4 for all of the flow geometries studied, again supporting the relative turbulent diffusion model. It can be argued that premixed flames at high Reynolds numbers behave like passive scalar surfaces due to the dominance of the turbulent convection process over the burning process. Therefore, one would expect the fractal dimension of premixed flames to asymptote at high Reynolds numbers to a value characteristic of passive scalar surfaces.

Since fractals have proven to be a useful tool for characterizing turbulent passive scalar surfaces, it has been suggested that they may be used to characterize premixed turbulent flame structure in the reaction sheet regime. It can be argued that flame surfaces propagate locally at the laminar flame speed, and that the turbulent fluctuations enhance flame speed mainly by convectively distorting the flame surface and thereby increasing the flame area. Fractal geometry can be used to characterize and predict the surface area of the flame. If the largest and smallest scales ( $\epsilon_i$  and  $\epsilon_o$  respectively) of wrinkling are known, the area enhancement, and by definition the turbulent to laminar flame speed ratio, can be predicted by using the power law description of fractals. This concept is represented by,

$$S_T/S_L = A_T/A_L = (\epsilon_i/\epsilon_o)^{2-D} \quad (3)$$

Gouldin [25] used the concept of fractal flame surfaces to introduce a model for turbulent premixed flame front propagation. He argued that in highly turbulent flows, the flame front could be treated as a passive scalar surface since the flame front motion would be dominated by the turbulent fluid motion. In this limit, he assumed that the fractal dimension of the flame structure was constant and equal to the passive scalar fractal dimension in turbulent flows, i.e. 2.37. For inner and outer cutoffs, he chose the Kolmogorov length scale,  $\eta$ , and integral length scale,  $L$ , respectively. With these assumptions, the model becomes



$$S_T/S_L = (\epsilon_t/\epsilon_o)^{2-D} = (\eta/L)^{2-D} \quad (4)$$

The ratio  $\eta/L$  can be represented by  $A_t^{-1/4} R_L^{-3/4}$  [26], where  $A_t$  is a constant of order one (in this case  $A_t$  was chosen as 0.37 based on pipe flow data), and  $R_L$  is the turbulent Reynolds number based on the integral length scale. Using this relationship, the turbulent to laminar flame speed ratio is given by

$$S_T/S_L = (A_t^{-1/4} R_L^{-3/4})^{2-D} \quad (5)$$

Gouldin noted that this relationship would not hold under conditions where the turbulence intensity to laminar flame speed ratio was small. Under such conditions, the smoothing of the wrinkled flame due to local burning becomes important and the flame surface cannot, therefore, be considered a passive scalar surface. Gouldin argued, however, that these effects would not change the fractal dimension, but would increase the inner cutoff since the small scales would be preferentially consumed by flame propagation. He proposed a relationship for the inner cutoff variation due to smoothing effects, as well as other modifications to account for flame stretch which will not be discussed here.

Alternatively, Kerstein [27] argues that flame surfaces cannot be considered passive scalar surfaces. The argument of flame surfaces being passive scalars at high turbulence Reynolds number relies on the argument that the time for the flame front to burn across an eddy of size  $\ell$  is  $\ell/S_L$ , where the eddy turnover time of  $(\ell/u')(L/\ell)^{1/3}$  is much shorter. Thus, the effect of laminar burning on the flame geometry is negligible. Kerstein argues that the proper velocity scale for burning across an eddy is  $S_T$  since the flame front within an eddy is wrinkled by smaller eddies. Based upon this argument, a theoretical value for the flame front fractal dimension of 7/3 is derived.

The first reported measurements [28] of the fractal nature of premixed flames were obtained during the first year of this program for turbulence Reynolds numbers below 100. The fractal dimensions obtained for these flames were approximately 2.1 and therefore much lower than the 2.37 estimate for passive scalar surfaces. The fractal dimension was also found to increase with increasing Reynolds number, although no functional relationship was developed since a very limited number of conditions were studied. A fractal dimension lower than the passive scalar fractal dimension was also obtained by Peters [29] using data from previously published two dimensional images: one image from an engine flame, one image from a V-flame. Fractal dimensions of 2.2, and 2.13 were obtained respectively, however, the turbulence conditions for these particular measurements were not given.

More recently, Mantzaras et al. [30,31], studying flames in engines, reported fractal dimensions near the passive scalar value of 2.35 for several cases at  $u'/S_L$  greater than 4. They also found that at  $u'/S_L$  equal to 0.5 the flame structure fractal dimension was reduced to approximately 2.1.

Lean methane bunsen burner flames have also been studied for fractal character by Murayama

and Takeno [32] and fractal dimensions below the passive scalar value of 2.35 observed. In particular, they reported a fractal dimension of 2.26 at a  $u'/S_L$  of 1.62.

An entirely different technique was used by Strahle [33] to calculate the fractal dimension of premixed turbulent flame fronts. The burned/unburned state of a stabilized turbulent conical flame was measured using Rayleigh scattering measurements, and the time history of these measurements related to the flame structure using Taylor's hypothesis. A fractal dimension can then be obtained from the crossing frequency using techniques which will not be discussed here. Analysis of this data produced a fractal dimension between 2.5 and 2.65, which is much higher than even the passive scalar fractal dimension. Similar results were obtained by Gouldin [34] for the flame crossing frequencies of rod stabilized V-flames. However, at the same turbulence conditions, two-dimensional images produced a fractal dimension of 2.1. This discrepancy in fractal dimensions between the crossing frequency and two-dimensional flame structure measurements may be evidence of the validity of the relative diffusion model. The crossing frequencies are single point measurements which are dominated by large scale motion of the flame front and the turbulent flow, hence the fractal dimension of the crossing frequency is related to that of the turbulent scales themselves, which is between 2.5 and 2.67 as discussed previously.

The results of all these measurements suggest that premixed turbulent flame structures are fractal over a broad range of turbulence Reynolds numbers throughout the reaction sheet regime, that the fractal dimension increases with increasing turbulence Reynolds number, and that the high Reynolds number limit corresponds to that of passive scalar surfaces. In order to develop a fractal turbulent flame speed model, the variation in flame structure fractal dimension with  $u'/S_L$  must be better understood. In this study extensive measurements of the fractal dimension of premixed turbulent flame structure have been made over a broad range of turbulence Reynolds and Damkohler numbers. Based on these measurements, a heuristic model has been developed which expresses the fractal dimension of the flame front in terms of the turbulence intensity to laminar flame speed ratio. The fractal dimension model has been used to predict turbulent flame speeds using equation 3 and these predictions are compared to other flame speed predictions.

The flame boundaries in the two dimensional flame structure images, such as those shown in Figure 11, may consist of a single line, or may be made up of a series of islands of burned and unburned gas. There are several methods which can be used to calculate the fractal dimension from the flame structure measurements. The most straightforward method consists of measuring the length of the curve using a range of scales, e.g. by stepping along the curve with calipers of fixed spacing and plotting the length obtained vs the caliper spacing for a range of caliper spacings. In practice, however, this technique does not result in a smooth straight line as shown in Figure 12, making it difficult to determine the fractal dimension (e.g. see reference 34). This is due to the fact that sections of the curve are omitted when a non-integer number of calipers "fit" on to a curve. This problem becomes less noticeable as the length of the curve becomes much longer than the outer

cutoff. In the case of the flame structure measurements, however, this is not possible and therefore other methods for calculating the fractal dimension are necessary. One such method is based on the two-dimensional autocorrelation of the perimeter [35] where  $\langle P(r)P(r+r) \rangle \propto r^{D-2}$ . This is actually equivalent to the caliper technique described above if for each caliper size, the procedure is repeated starting at all points along the length of the curve. Another method which can be used to calculate the fractal dimension, and the one used in this study, utilizes an area calculation procedure [36]. In this method, the area encompassed by strips of width,  $\epsilon$ , on both sides of the curve is calculated. This area,  $A$ , is equal to  $2\epsilon L$ , which from equation 1 implies that

$$A \propto \epsilon^{2-D} \quad (6)$$

Using this method, the area vs. measurement scale curve is very smooth and allows for a simple and unambiguous determination of the fractal dimension. In this study, the area calculated for each scale was divided by  $2\epsilon$  to produce plots of  $\log(L)$  vs  $\log(\epsilon)$ , where the slope is then equal to one minus the fractal dimension.

Each of the two-dimensional flame structure images was analyzed using the fractal algorithm described above. Three typical fractal plots are shown in Figure 13, one at each of the conditions shown in Figure 11. The characteristics of this plot will be examined relevant to the previous discussion.

As can be seen in Figure 13, there is a range of scales over which the slope is constant for each flow condition, which is a necessary and sufficient condition to show that these flame structure measurements display fractal character. The flame surface fractal dimension is simply one minus the slope of these curves. The values of fractal dimension calculated from the individual fractal plots in Figure 13 are 2.23, 2.24, and 2.36 for  $u'/S_L$  values of 0.60, 1.47, and 11.9, respectively. The fractal dimensions for all of the flame structure measurements at a given  $u'/S_L$  were averaged and the results obtained over the range of conditions tested plotted in Figure 14, where the vertical bars on each data point represent one standard deviation from the mean of the sample obtained at each  $u'/S_L$ . The average fractal dimension is shown to increase with increasing  $u'/S_L$  and to approach limiting values at both low and high  $u'/S_L$ . At low  $u'/S_L$ , the flame surface fractal dimension does not appear to be approaching 2.0, the Euclidean dimension of a plane, as expected. Instead, the fractal dimension is apparently approaching a slightly larger value. This behavior is most likely due to flame front instabilities, and perhaps a coupling with the turbulence. At high  $u'/S_L$  the fractal dimension appears to be approaching a limiting value between 2.3 and 2.4. This will be discussed in more detail later.

The variation in the fractal dimension among individual flames at the same  $u'/S_L$  is not due to measurement uncertainty, but is a real characteristic of the turbulent flame structure. This is illustrated by the two dimensional images shown in Figure 15 which correspond to the minimum, average, and maximum fractal dimension measurements for  $u'/S_L = 4.8$ . The results shown in Figure 14 indicate that the variation in flame structure fractal dimension increases with increasing  $u'/S_L$ .

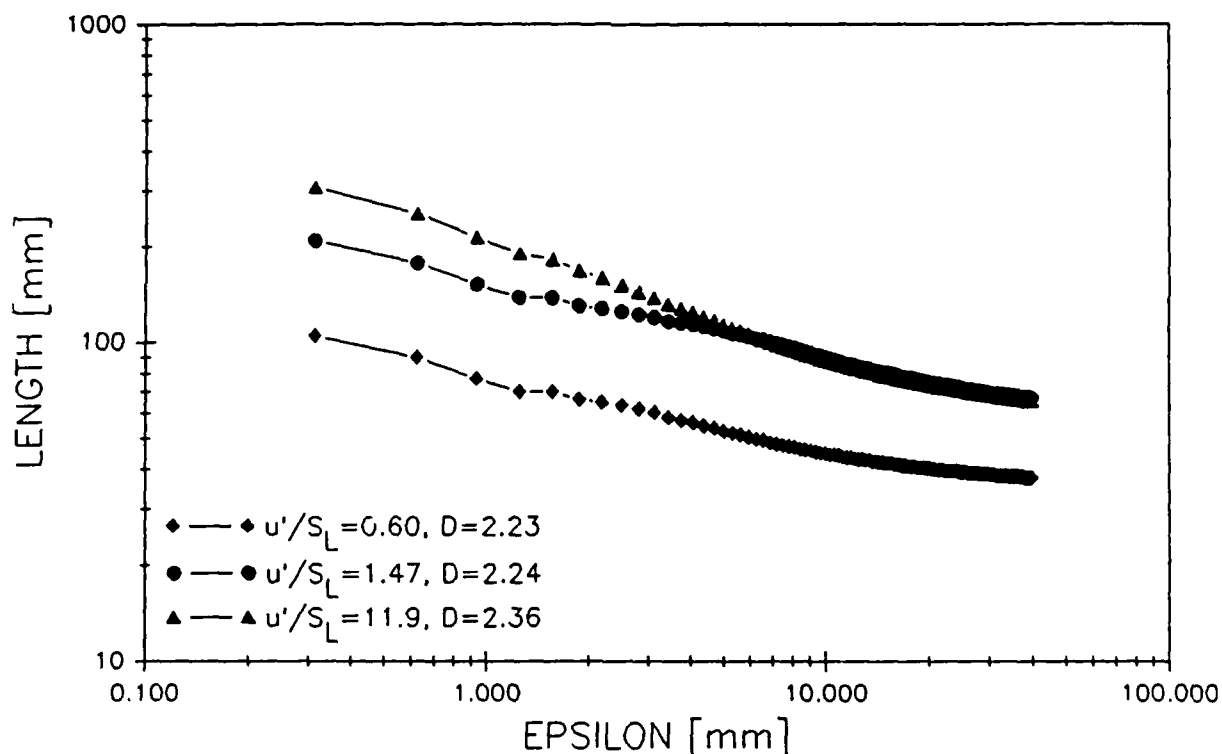


Figure 13. Plot of the fractal character of an individual flame front at three different conditions.

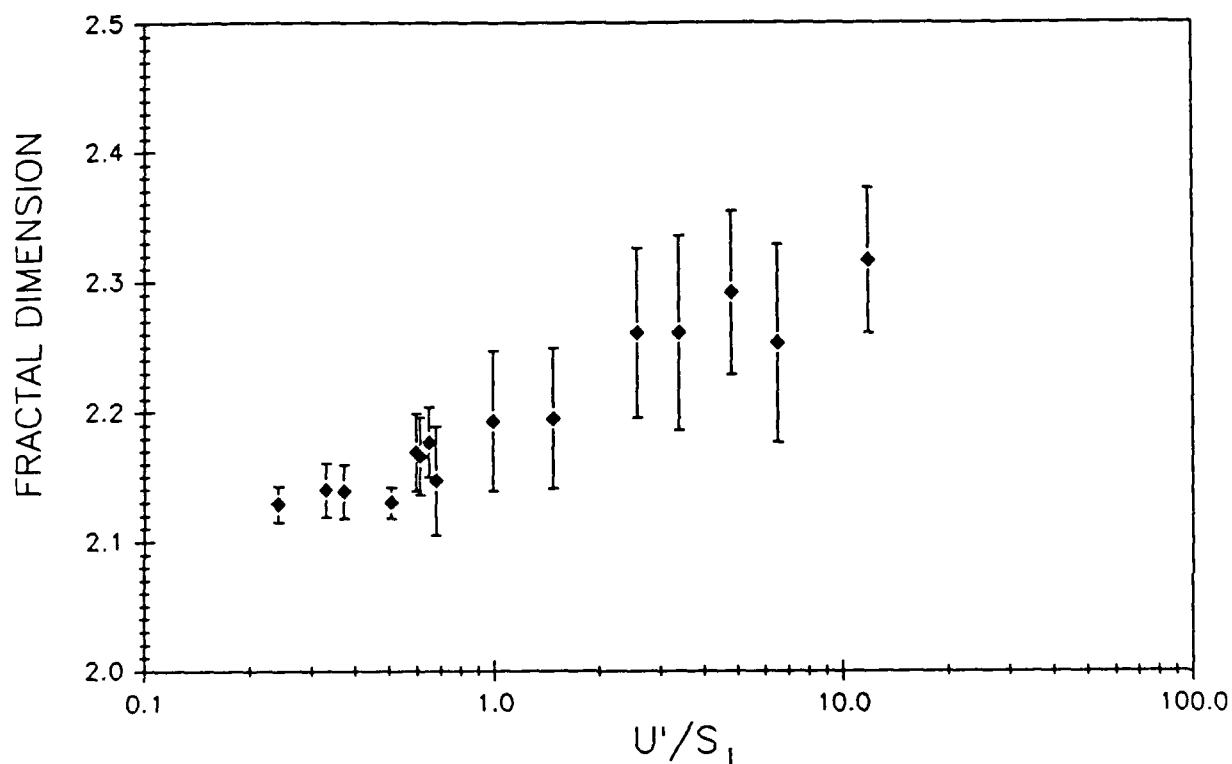
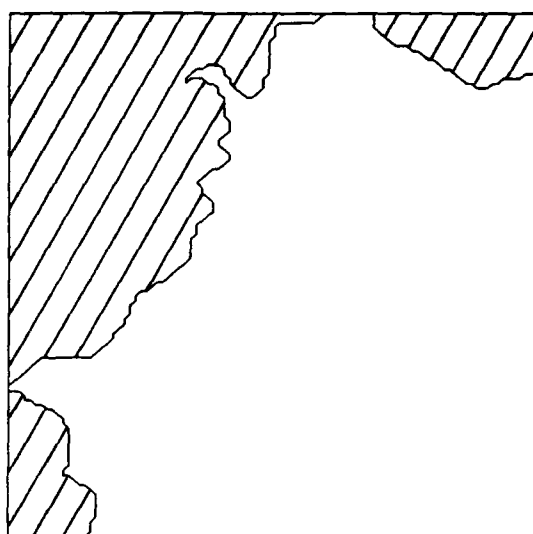
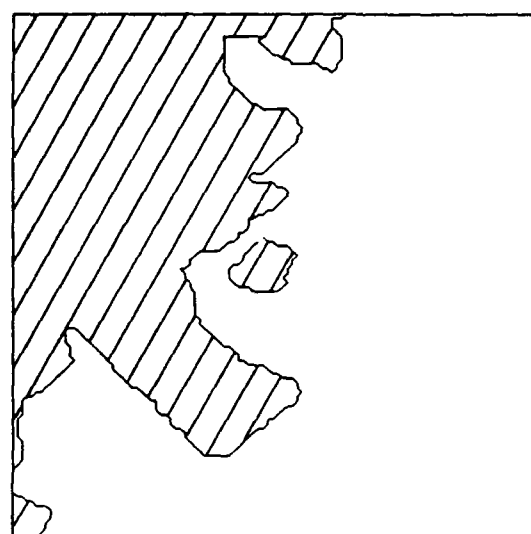


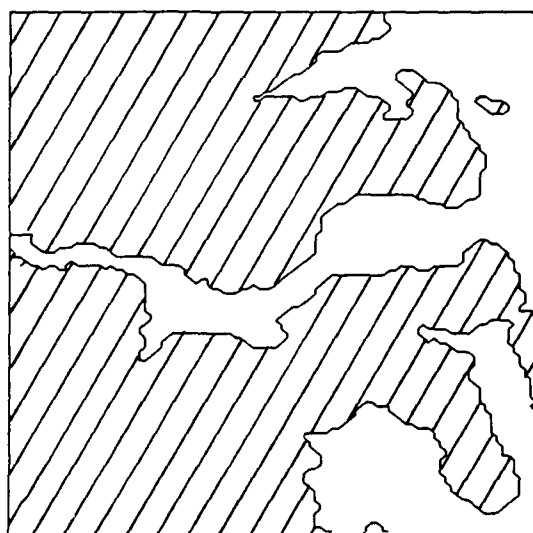
Figure 14. Average and standard deviation of the fractal dimensions obtained at each flow condition.



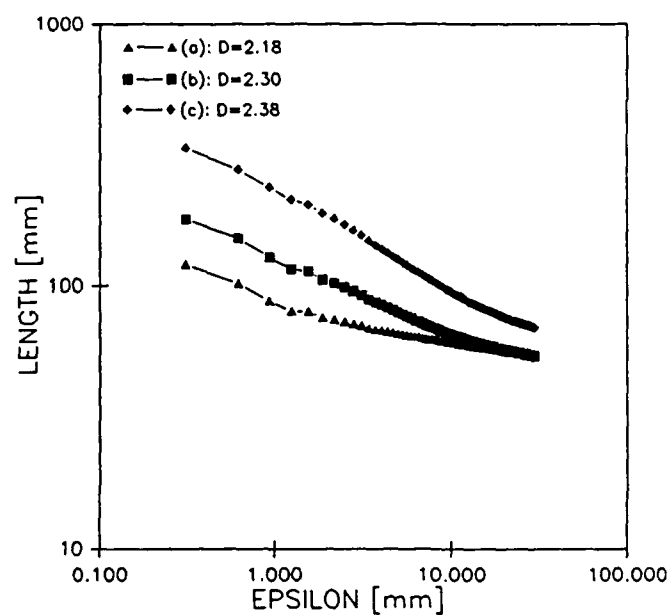
(a)



(b)



(c)



(d)

Figure 15. Flame structure images at  $u'/S_L = 4.8$ , with the maximum, average, and minimum fractal dimensions (a,b,c) and corresponding fractal plots (d).

and that the magnitude of the observed variation is comparable to the entire range of fractal dimensions. At this time, the cause of this behavior is not fully understood.

The outer cutoff can be identified in Figure 13 as the point where the curve deviates from the constant slope region. This quantity is important since it is required to determine the turbulent flame speed using equation 3. Figure 13 shows that the outer cutoff is not a sharp cutoff as illustrated in Figure 12, but that there is a gradual transition. The transition, however, does occur over a narrow range of scales comparable to the integral scale for the flow conditions studied. For this reason, the integral length scale will be used as the outer cutoff when predictions of turbulent flame speed are made.

The inner cutoff is also required in equation 3 to calculate the turbulent flame speed. The measurements in this study, however, have not been made with sufficient spatial resolution to determine the inner cutoff from the fractal analysis. In order to experimentally evaluate the inner cutoff, changes must be made to the experimental system, including narrowing the laser sheet and increasing the pixel resolution of the camera. Based on physical arguments, there are several hypotheses regarding the proper physical scale which should be used to represent the inner cutoff including the Kolmogorov length scale, the laminar flame thickness, and a quantity called the Gibson scale [29]. However, since the smallest scales of wrinkling are a manifestation of the interaction between the small scale turbulent eddies and the local flame front, a process which is not well understood at this time, no conclusive statements can be made regarding the correct choice for the inner cutoff.

The simplest argument is that the smallest scale of wrinkling corresponds to the Kolmogorov scale, which is the smallest scale of turbulence present in the flow. There are several other factors, however, which must be considered. First, Gouldin [24] argues that while the Kolmogorov scale may be the proper inner cutoff at high turbulence intensities, the smoothing action of flame propagation preferentially consumes the small scales at low turbulence intensities, which effectively raises the inner cutoff. Second, Peters [29] argues that only scales which take longer than one eddy rotation period to pass through the flame front can alter the structure of the flame. Eddies smaller than this are not capable of depositing appreciable energy in the flame zone to produce wrinkles. This scale is called the Gibson scale. Third, at high values of  $u'/S_L$ , the Kolmogorov scale can become smaller than the laminar flame thickness. A simple thought experiment shows that it is impossible for a surface to have wrinkles which are smaller than the surface thickness. Under such conditions, the laminar flame thickness would be a more reasonable choice for the inner cutoff. Recent results in lean methane-air premixed flames with a  $u'/S_L$  of 1.62 have, in fact, showed an inner cutoff near  $\delta_L$ , which in this case was an order of magnitude greater than  $\eta$  [32] due to the lean operating conditions. Note, however, that at levels of turbulence where the laminar flame thickness is greater than the Kolmogorov length scale, the reaction sheet assumptions begin to breakdown, which may invalidate the fractal flame front analysis.

In order to account for the smoothing action of flame propagation on the inner cutoff, Gouldin [24] assumes that as  $u'/S_L \rightarrow 0$ ,  $\epsilon_i \rightarrow \epsilon_0$ , since  $S_T \rightarrow S_L$  and proposes a simple correction factor

to predict this behavior. At our lowest Reynolds number case of 35, where this phenomenon would be most important, the correction factor suggested by Gouldin would raise the inner cutoff from the calculated Kolmogorov length scale of  $500\mu\text{m}$  to approximately  $35\text{mm}$ , which is larger than the largest scales of turbulence found in the flow. Clearly this cannot be the case, and some modification to this approach is necessary.

Peters [29] suggests that the smallest scale of wrinkling is defined by the smallest turbulence scales which remain in the reaction region long enough to alter the flame structure, which he argues could be represented by the relationship,

$$L_G = L \cdot (S_L/u')^3 \quad (7)$$

where  $L_G$  is the Gibson scale. Note that when  $u'/S_L$  is less than unity,  $L_G$  is larger than the integral scale,  $L$ , which implies that the flame front cannot be wrinkled by any scales present in the flow. Experimental evidence, however, has shown that at  $u'/S_L$  less than unity, flames still exhibit wrinkling, as shown in Figure 11, and that the fractal character extends to scales smaller than the integral scale, as shown in Figure 13. At values of  $u'/S_L$  between 1 and 6, the Gibson scale varies between the  $L$  and  $\eta$ , however, and no evidence of an inner cutoff corresponding to  $L_G$  was observed in this regime.

Each of the inner cutoff proposals discussed above appears to be implausible at some range of turbulence intensity. Those that take into account flame dynamics (i.e. Peters and Gouldin), while they may be valid at high  $u'/S_L$ , appear to overestimate the inner cutoff at low turbulence intensity. However, simple estimates of the inner cutoff, such as  $\eta$  and  $\delta_L$ , do not take into account the smoothing action of flame propagation or the fact that these scales may be incapable of depositing enough energy to alter the flame front structure. Since there is no clear evidence of an inner cutoff down to the  $300\mu\text{m}$  spatial resolution of the reported measurements,  $\eta$  will be used as the inner cutoff in the turbulent flame speed predictions which are presented. Currently experimental design changes are being implemented to allow an order of magnitude increase in the spatial resolution of the two dimensional flame structure measurements, which will allow direct measurement of the inner cutoff.

As discussed earlier, at high Reynolds numbers, it is expected that the flame front will behave dynamically as a passive scalar surface. This occurs since the burning process is dominated by the turbulent convective action. As previously discussed, the passive scalar fractal dimension has been determined to be approximately 2.35. In this study, the flame structure fractal dimension is found to approach this value at values of  $u'/S_L$  greater than 10. This supports the argument that at high Reynolds numbers, the flame front behaves as if it were a passive scalar surface.

It should be noted again, however, that Kerstein [27] has recently argued that the upper limit of the fractal dimension of premixed flames is not related to the fractal dimension of turbulent passive scalars, but instead to the dynamics of flame propagation. The upper limit of the fractal dimension of flame surfaces can then be shown to be  $7/3$ . Unfortunately, since this value is

effectively the same as the expected fractal dimension for passive scalar surfaces, the results of this study cannot be used to resolve this issue.

The results of this study shown in Figure 14 clearly indicate that the fractal dimension increases with increases in the turbulence intensity to laminar flame speed ratio. This can be explained in terms of two competing processes. First, the turbulent velocity fluctuations act to convectively distort the flame front at a rate proportional to the characteristic velocity scale,  $u'$ . Second, the laminar burning process acts to smooth the flame surface at a rate proportional to the laminar burning speed,  $S_L$ . The relative importance of these processes changes with  $u'/S_L$ , where the smoothing process dominates at low values, and turbulence dominates at high values. In the region between these two limits, both effects are important.

In order to quantify this behavior, a heuristic model for the fractal dimension of flame surfaces has been developed [37]. The rate of wrinkling is represented by  $u'$ , which accounts for the tendency of the turbulent motion to distort the flame surface into a passive scalar with a fractal dimension  $D_T$ . The rate of smoothing is represented by  $S_L$ , which represents the tendency of the burning process to eliminate wrinkles from the flame surface, thereby lowering the fractal dimension, towards a laminar limit,  $D_L$ . The combined effect of these processes is represented by the equation:

$$D_F = \frac{S_L}{u' + S_L} D_L + \frac{u'}{u' + S_L} D_T, \quad (8)$$

or

$$D_F = D_L / (u'/S_L + 1) + D_T / (1 + S_L/u')$$

where  $D_F$  refers to the flame surface fractal dimension,  $D_L$  refers to the fractal dimension which the flame surface would assume in the absence of turbulence, and  $D_T$  refers to the fractal dimension of a passive scalar surface. Based on earlier arguments, values of 2.05 and 2.35 have been used for the laminar flame fractal dimension and turbulent passive scalar fractal dimension, respectively. Figure 16 shows a comparison between this model and the fractal dimension measurements from this study, as well as those from Mantzaras et al. [30,31] and Murayama and Takeno [32]. The heuristic model appears to agree well with the measured flame surface fractal dimensions over the entire range of  $u'/S_L$  from the laminar limit to the high Reynolds number limit.

The heuristic fractal dimension model can be used in equation 3 to obtain an expression for the turbulent to laminar flame speed ratio which is a function of the turbulence intensity to laminar flame speed ratio, and the inner to outer cutoff ratio. Assuming that the inner and outer cutoffs are the Kolmogorov and integral scales, respectively, then the turbulent to laminar flame speed ratio becomes a function of the turbulence intensity to laminar flame speed ratio, and the Kolmogorov to integral length scale ratio. Physically, the dependence on  $u'/S_L$  reflects the competition between



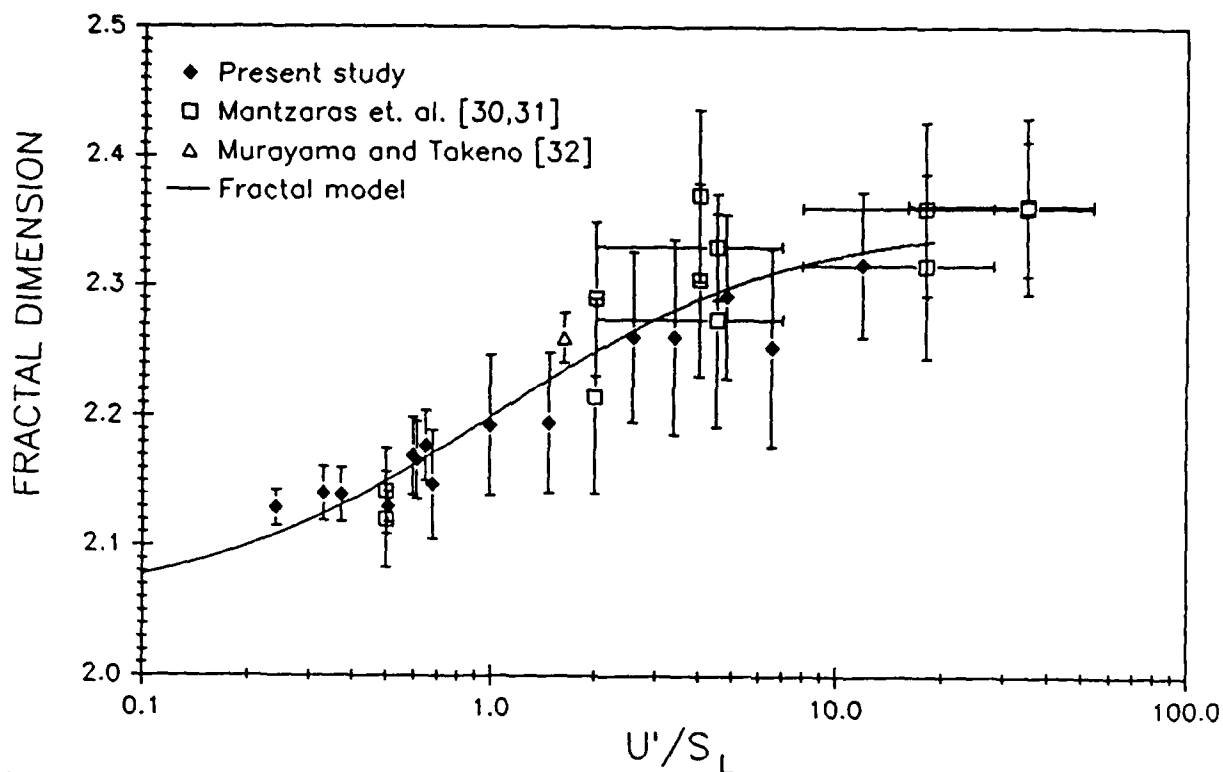


Figure 16 Comparison of fractal dimensions predicted by heuristic model and experimentally measured values.

convective distortion and smoothing of the flame front, and as a result defines the fractal dimension or the distribution of scales in the flame structure; while the Kolmogorov and integral scales define the range of scales.

A number of turbulent flame speed models have been developed for the reaction sheet regime of premixed turbulent flame propagation [38-42]. These models can basically be grouped into two categories, those that predict a linear dependence on  $u'/S_L$  and those that predict a dependence on  $\sqrt{u}/S_L$ , while none of the models explicitly account for length scale. These models are compared in Figure 17, along with the predictions of the fractal flame speed model. Since the fractal flame speed model is a function of  $u'$ ,  $S_L$  and  $L$  the comparison shown in Figure 17 is for a specific  $S_L$  and  $L$ , i.e. 40 cm/sec and 8.2mm, respectively. As shown, there is good agreement between the fractal model and the Clavin-Williams model [42]. The Clavin-Williams model, however, does not account for the independent effects of  $S_L$  and  $L$  for a given  $u'/S_L$ , which the fractal flame speed model includes. This is illustrated in Figure 18, where  $S_T/S_L$  is plotted versus  $u'/S_L$  for various values of  $L$ . The fact that the turbulent to laminar flame speed ratio depends independently on  $u'$ ,  $S_L$  and  $L$  is an important result of the fractal turbulent flame speed model and one which must be allowed for when attempting to properly correlate turbulent flame speed measurements. Failure to do so may partially explain the wide variations in reported turbulent flame speed measurements.

Validation of the fractal turbulent flame speed model through comparison with measured turbulent flame speeds is an important test. Despite the abundance of reported turbulent flame

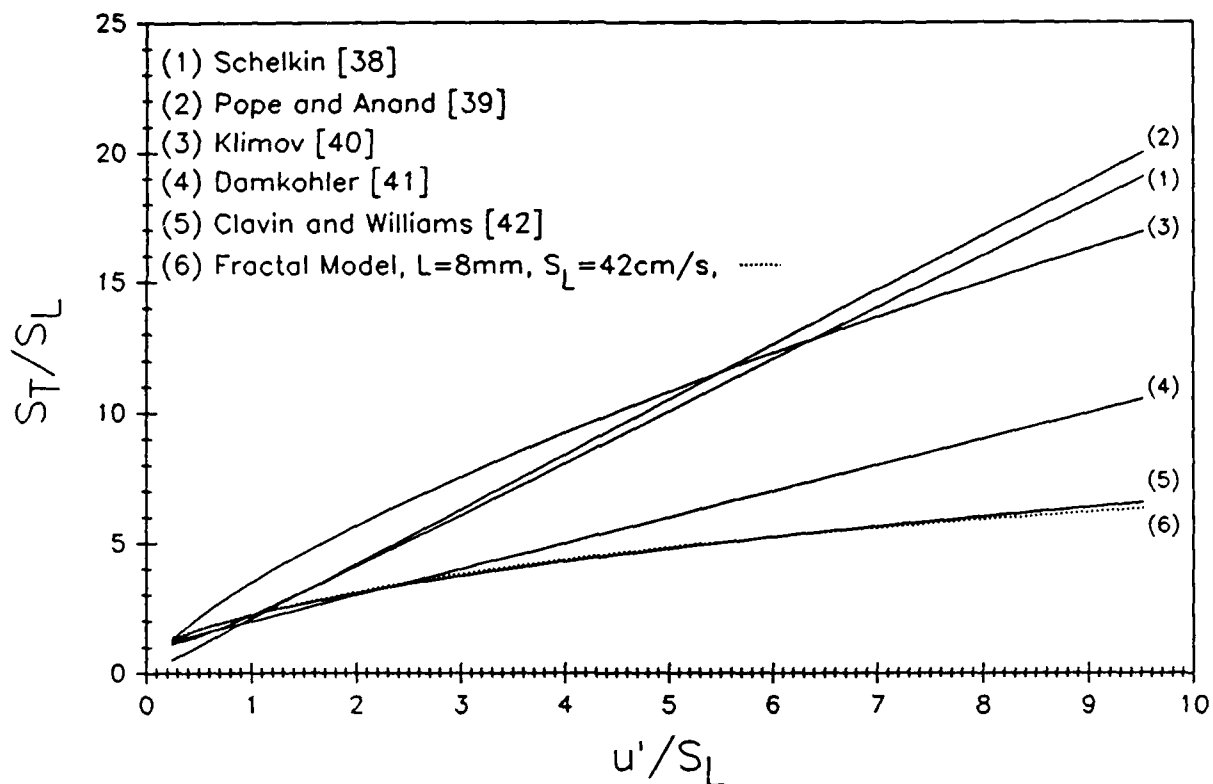


Figure 17. Comparison of flame speed predicted by fractal model with several other reaction sheet models.

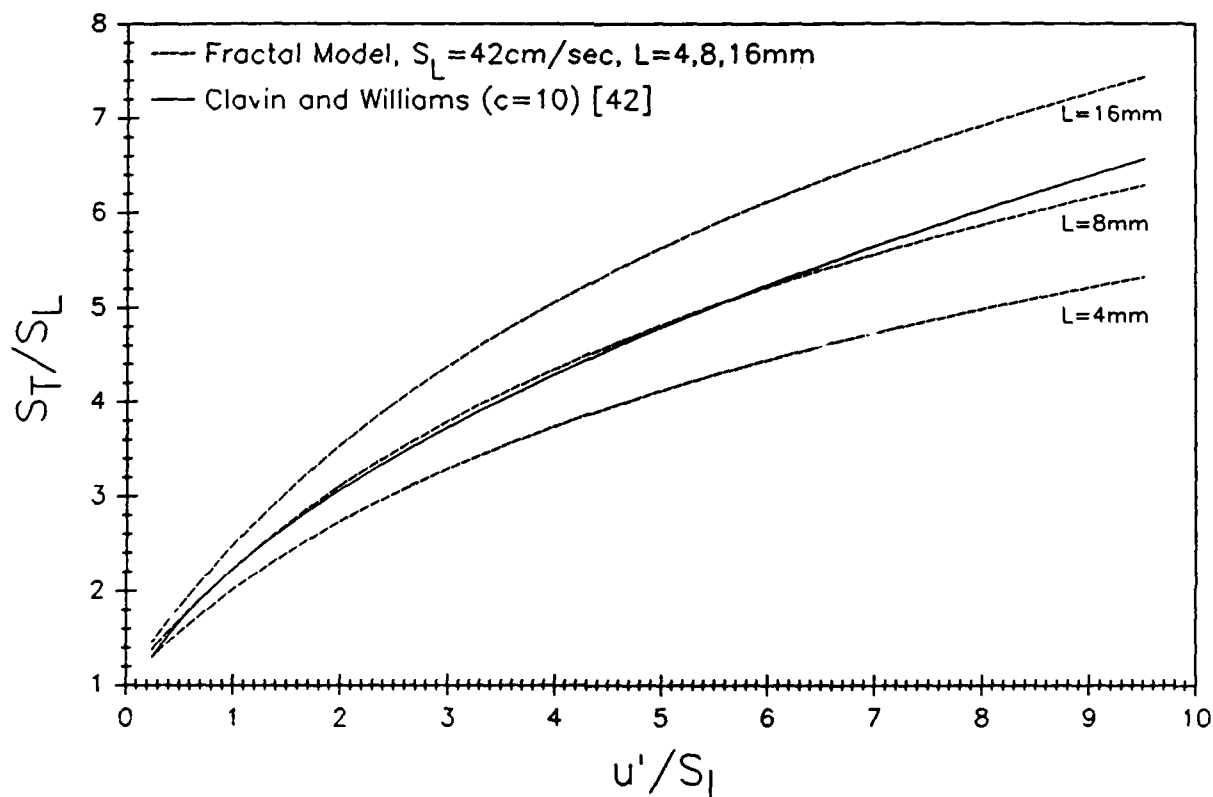


Figure 18. Comparison of flame speeds predicted by the fractal model at different integral length scales with Clavin and Williams model.

speed data, there are two important limitations to most of the measurements which preclude their use for this purpose. One limitation is the absence of information on the turbulent length scale which, as illustrated in Figure 18, has a significant effect on the turbulent flame speed. The second limitation pertains to unwanted flow field effects associated with the various flame configurations, as discussed previously, including the effects of the stabilization mechanism, free stream shear and restrictions in the burned gas flow. These phenomena can actually affect the flame structure and, in turn, the flame speed over and above the effect of the incident turbulent flow. Another factor which complicates the measurement of turbulent flame speeds is the uncertainty in defining the flow direction of the unburned gas with respect to the mean flame front. Although the freely propagating, planar flame configuration used for the flame-generated turbulence and the flame structure measurements is not affected by the unwanted flow field effects described above, the definition of the upstream flow with respect to the mean flame front is still a problem. In fact, it is a greater problem than in the various stabilized flame configurations. The flame configuration, which is not subject to any of these problems, is the freely propagating spherical flame [43]. In this case, however, the flame propagation rate undergoes a transition from an initially laminar growth rate to a fully developed turbulent growth rate. This process is accounted for in the turbulent flame kernel model described in the following section, which incorporates the heuristic flame structure fractal dimension model and the fractal flame speed model. The ability of the turbulent flame kernel model to predict the transition from a laminar to a fully developed turbulent flame is actually a more rigorous test of the fractal flame speed model. Unfortunately, there are very few experimental measurements of turbulent flame kernel growth. At the end of the next section comparisons are made with the very limited amount of data which is available.

### Turbulent Flame Kernel Growth Model

The results which have been obtained regarding the fractal nature of premixed turbulent flames have been used to develop a fractal based model of turbulent flame kernel growth [44]. The three processes which govern spark ignited flame kernel growth are gas breakdown, flame propagation and thermal expansion. The initial gas breakdown process affects the growth rate in that it determines the initial size, temperature and composition of the flame kernel, where the initial size affects the kernel's susceptibility to the effects of turbulence and the initial temperature and chemical composition affect the initial laminar flame speed. Thermal expansion refers to the expansion of the flame kernel required to accommodate the flame's chemical heat release and additional energy supplied by the ignition system, for example, during a long duration glow discharge. The specific aspect of flame kernel growth which is accounted for in this model is that due to flame propagation and specifically the effect of turbulence on that process. In the absence of additional ignition energy following gas breakdown, the growth rate,  $\dot{R}$ , of a spherical flame kernel is related to the flame speed by the following expression:

$$\dot{R} = \frac{\rho_u}{\rho_b} S \quad (9)$$

where  $\rho_u$  and  $\rho_b$  are the unburned and burned gas densities, respectively, and  $S$  is the laminar or turbulent flame speed. In the case of a laminar flame kernel,  $R$  is the actual kernel radius, while in the case of a turbulent flame kernel  $R$  represents an equivalent flame kernel radius. This expression accounts for both flame propagation and the thermal expansion due to the flame's chemical heat release.

The effect of the turbulence on flame kernel growth, as represented by equation 9, is through changes in the flame speed,  $S$ . The fundamental effects of turbulence on flame speed are much the same in a flame kernel as in a fully developed flame, where turbulence scales which are larger than the laminar flame thickness act to convectively distort or wrinkle the flame surface. This increases the flame's surface area, and, as a result, the overall mass burning rate. On the other hand, turbulence scales which are smaller than the laminar flame thickness effectively increase the transport rates within the flame front and thereby increase the local burning rate. The local burning rate can also be affected by local flame stretch, where, for example, sufficiently intense turbulence can actually result in local extinction of the flame.

The major difference between a fully developed turbulent flame and a turbulent flame kernel is that the flame kernel imposes its own characteristic time and length scales, i.e. the kernel lifetime and size, respectively. To properly account for these characteristic time and length scales, it is necessary to allow for the fact that the turbulent flow consists of a range of time and length scales and that only those turbulence scales which are smaller than the kernel's characteristic scales can affect the kernel growth rate. Therefore, the effect of turbulence actually increases with time until the kernel's characteristic time and length scales exceed the largest turbulence scales. During the

transition to fully developed turbulent growth, the kernel's growth rate is a function of both the kernel lifetime and size.

One approach which has been used to account for the range of turbulence time scales affecting flame kernel growth is based on the use of the turbulence energy spectrum [45]. In this approach, the time scale of the flame kernel, i.e. its lifetime, is directly compared to the distribution of turbulence time scales represented by the turbulence energy spectrum. It is assumed that the only frequencies which can affect the flame kernel growth rate are those greater than the reciprocal of the flame kernel lifetime. As the time following ignition increases, the portion of the turbulence energy spectrum which affects flame kernel growth increases. This is illustrated in Figure 19, where the effective turbulence intensity at a particular time,  $t$ , is defined by the square root of the area under the energy spectrum over the range of frequency components greater than the reciprocal lifetime, i.e.

$$u(t)^2 = \int_{1/t}^{\infty} E(f) df \quad (10)$$

One can then use this effective turbulence intensity along with conventional turbulent flame speed correlations to predict the turbulent flame speed versus time for the growing flame kernel.

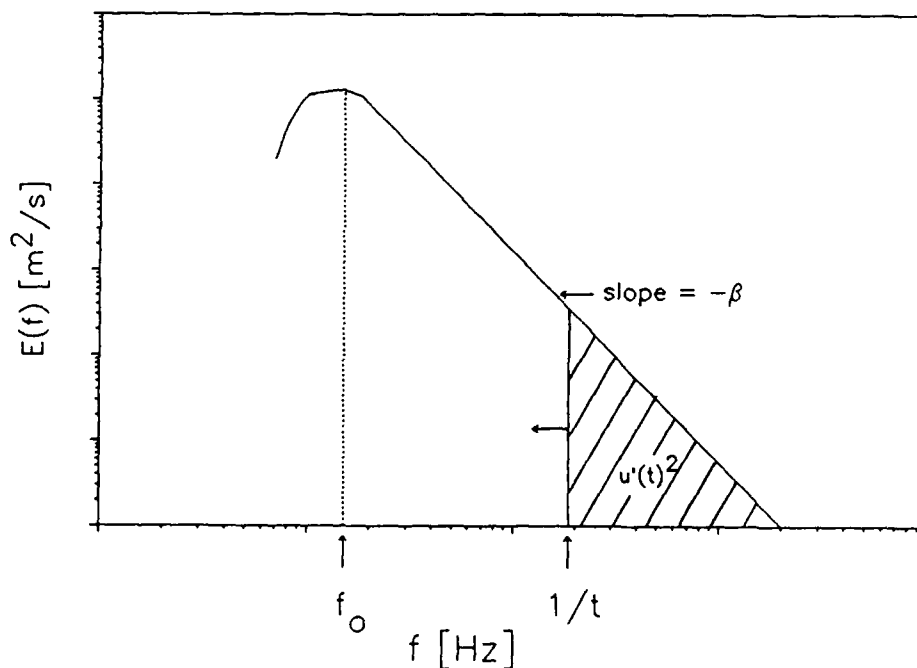


Figure 19. Turbulence energy spectrum.

There are two limitations, however, to this approach. One is that it does not account for the important role of turbulence length scales. The second is that it relies on the use of existing empirical or theoretical flame speed correlations which to date vary widely from experiment to experiment or model to model. Using the fractal flame speed model which was presented in the previous section, a turbulent flame kernel growth model has been developed which accounts for the effects of both time and length scales.

As discussed in the previous section, the turbulent to laminar flame speed ratio is given by

$$S_T/S_L = \left[ \frac{\eta}{L} \right]^{2-D} \quad (11)$$

where the Kolmogorov and the integral scales have been taken to be the inner and outer cutoffs, respectively, and the fractal dimension is given by the heuristic model

$$D_f = \frac{u'}{u' + S_L} D_r + \frac{S_L}{u' + S_L} D_L \quad (12)$$

For the case of a spherical flame kernel the laminar limit,  $D_L$ , is taken as 2.0, while the high Reynolds number limit,  $D_r$ , is taken at 2.35, as discussed previously.

In order to account for the effect of time scales on turbulent flame kernel growth, equation 10 can be used to define an instantaneous or effective turbulence intensity. In this case the effective turbulence intensity can be approximated by,

$$\begin{aligned} u'(t) &= u_o (f_o t)^{\frac{\beta-1}{2}} & t \leq 1/f_o \\ u'(t) &= u_o & t \geq 1/f_o \end{aligned} \quad (13)$$

where  $\beta$  is the slope of the energy spectrum and  $f_o$  is the low frequency limit of the energy spectrum. The instantaneous turbulence intensity can then be used to define an instantaneous fractal dimension using equation 12.

$$D_f(t) = \frac{S_L}{u'(t) + S_L} 2.0 + \frac{u'(t)}{u'(t) + S_L} 2.35 \quad (14)$$

Again, equation 14 accounts for the effects of turbulence, which acts to wrinkle the flame kernel, and burning, which acts to smooth the flame kernel. However, by using the effective turbulence intensity only the turbulence motion which has had sufficient time to wrinkle the flame surface is accounted for. Note that it is assumed that the flame kernel structure is fractal during the transition to a fully developed turbulent structure.

The instantaneous fractal dimension can then be used to predict the instantaneous turbulent flame speed using equation 11. One must also, however, account for the fact the flame kernel surface cannot exhibit scales larger than its size. In fact, a reasonable approximation is that the largest scale of wrinkling is equal to half the kernel radius. This gives the following equations for the turbulent flame speed.

$$S_T(t) = S_L \left[ \frac{\eta}{R(t)/2} \right]^{2-D(t)} \quad R(t) \leq 2L$$

$$S_T(t) = S_L \left[ \frac{\eta}{L} \right]^{2-D(t)} \quad R(t) \geq 2L$$
(15)

Finally, the instantaneous turbulent flame speed given by equation 15 can be used in equation 9 to determine the instantaneous growth rate, which, when integrated from the initial kernel radius,  $R_0$ , gives the kernel radius as a function of time.

Figures 20 and 21 show the results of an example calculation for the case of  $u' = 1.0$  m/s,  $S_L = 0.3$  m/s,  $\beta = 5/3$ ,  $f_0 = 100$  Hz,  $\eta = 0.4$  mm,  $L = 10$  mm,  $R_0 = 3$  mm, and  $\rho_u/\rho_b = 6.0$ . Figure 20 is a plot of the flame kernel radius as a function of time, which shows the transition from an initial laminar growth rate to a fully developed turbulent growth rate. This is shown more clearly in Figure 21, where the instantaneous flame kernel growth rate,  $\dot{R}(t)$ , is directly compared to the laminar and the fully developed turbulent growth rates for these particular conditions.

As discussed previously, the flame configuration which provides the most meaningful measurement of turbulent flame speed is a freely propagating, spherical flame. Therefore, comparisons between the fractal turbulent flame kernel model and actual turbulent flame kernel growth measurements are needed in order to evaluate the use of fractals to characterize and predict turbulent flame propagation. Unfortunately, there are very few turbulent flame kernel growth measurements available for this purpose. Figures 22 and 23 show two such comparisons. Figure 22 shows a comparison with measurements made in a high velocity turbulent flow such that the flame kernel rapidly detaches itself from the spark electrodes [46]. In this particular case, the agreement between the model prediction and the measurement is very good. Another comparison, shown in Figure 23, was made with measurements obtained in the pulsed-flame flow reactor at Penn State using the laser shadowgraph technique described previously. These measurements were obtained under significantly different turbulence conditions, for 0, 15 and 30% nitrogen dilution and with laser spark ignition [47]. Again, the model gives good agreement with the measured kernel growth. However, there does appear to be a difference in the initial growth rate, especially for the high dilution case. This is most likely due to an enhanced initial laminar flame speed due either to the high initial temperature or radical composition of the flame kernel following gas breakdown [48].

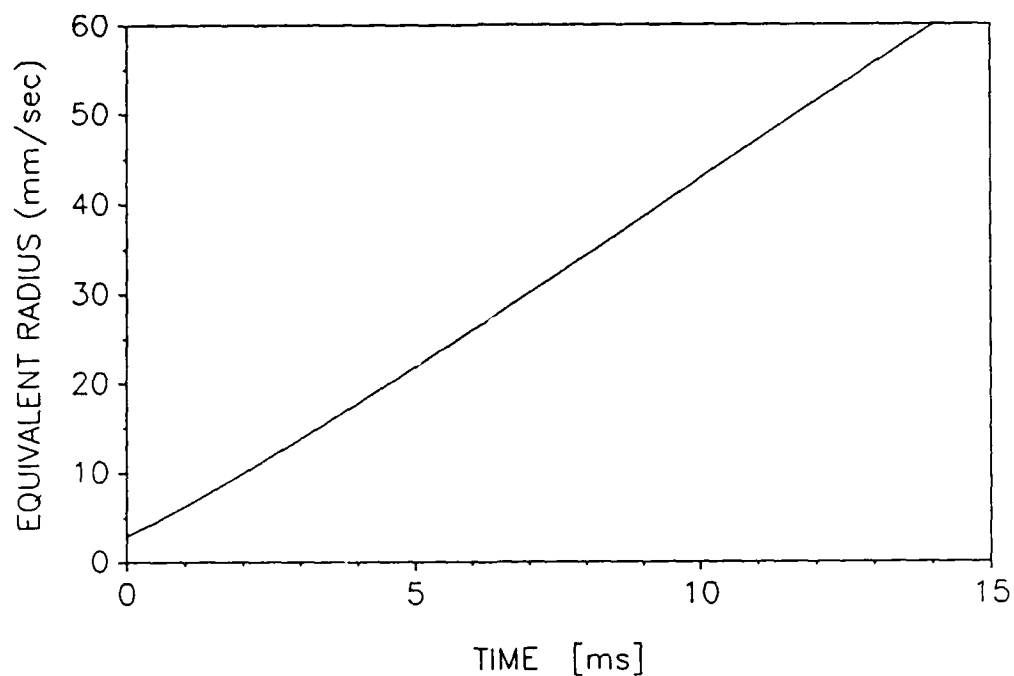


Figure 20 Fractal turbulent flame kernel model calculation for  $u' = 1$  m/s,  $\beta = 5/3$ ,  $f_0 = 100$  Hz,  $\eta = 0.4$  mm,  $L = 10$  mm,  $S_L = 0.3$  mm.

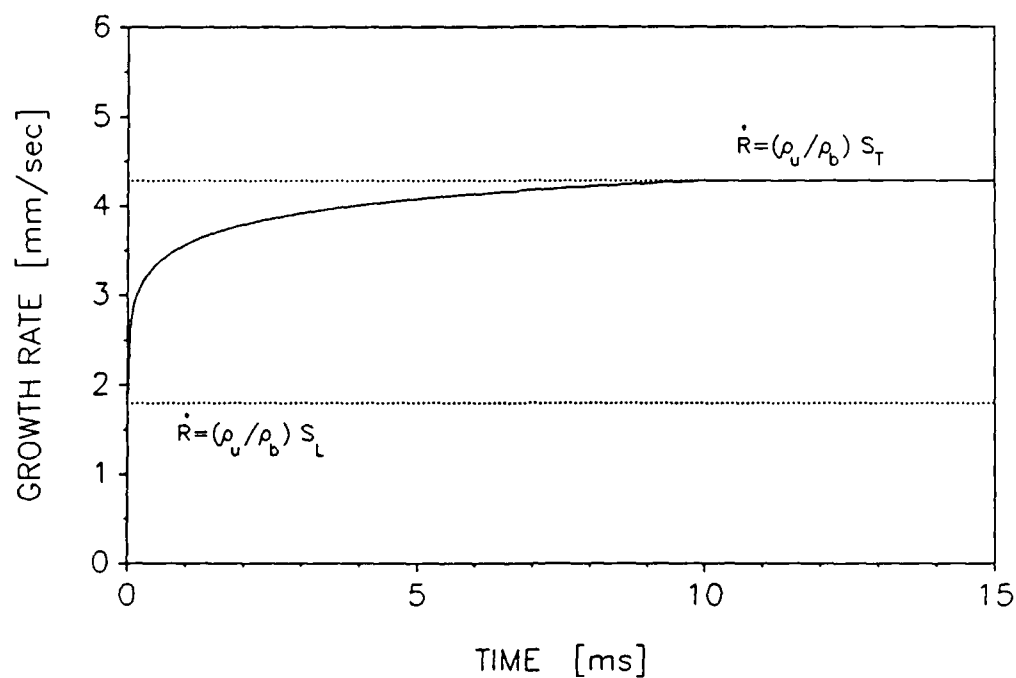


Figure 21 Fractal turbulent flame kernel model calculation for  $u' = 1$  m/s,  $\beta = 5/3$ ,  $f_0 = 100$  Hz,  $\eta = 0.4$  mm,  $L = 10$  mm,  $S_L = 0.3$  m/s.



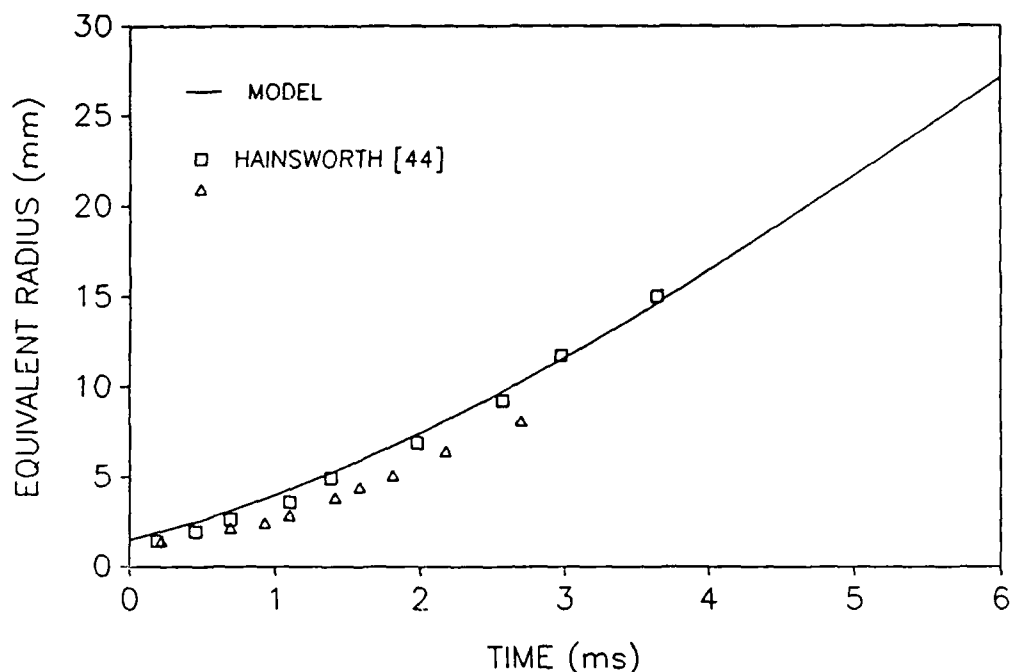


Figure 22. Comparison between fractal model turbulent flame kernel model and measurement of Hainsworth[44].

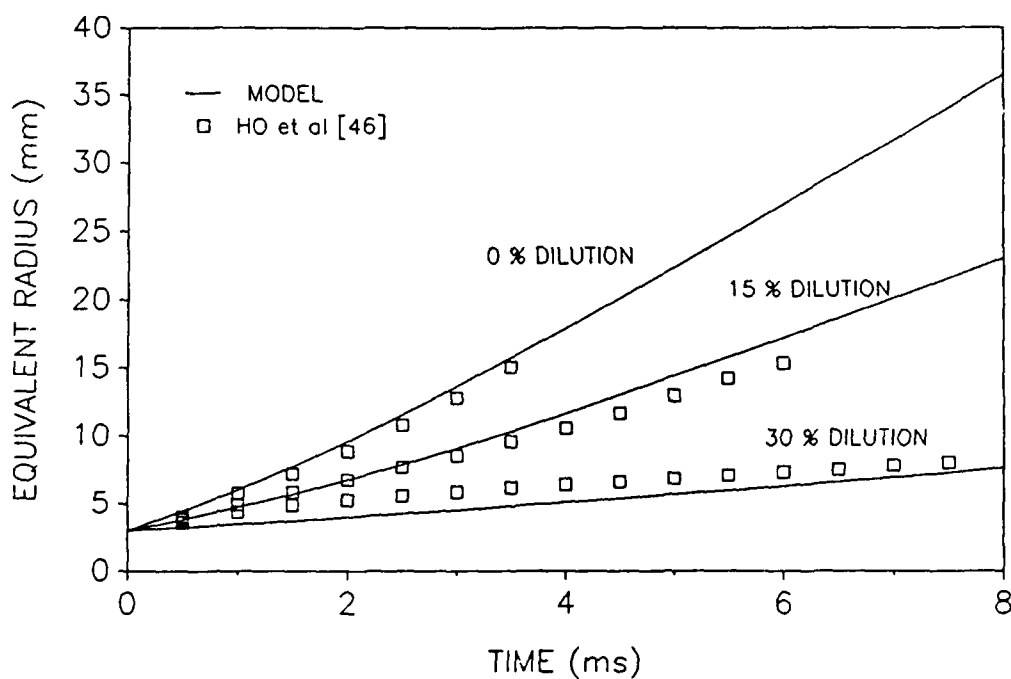


Figure 23. Comparison between fractal turbulent flame kernel model and measurements of Ho et al.[46].

Measurements have recently been initiated using two-dimensional fluorescence measurements of OH radical concentration and gas temperature in order to address this important question [49].

Although the comparisons shown in Figures 22 and 23 are very encouraging, a much more comprehensive evaluation of the fractal turbulent flame kernel model over a broad range of turbulence conditions is still required. Such measurements will be made in the pulsed-flame flow reactor.

## References

1. Bill, R. G., Namer, I., Talbot, L., Cheng, R. K., and Robben, F., Combustion and Flame, Vol. 43, p. 229 (1981).
2. Dandekar, K. V. and Gouldin, F. C., AIAA Journal, Vol. 20, No. 5, p. 652 (1982).
3. Cheng, R. K. and Ng, T. T., Combustion and Flame, Vol. 52, p. 185 (1983).
4. Cheng, R. K., Combust. Sci. Tech., Vol. 41, p. 109 (1984).
5. Golkalp, I., Shephard, I. G. and Cheng, R. K., Combustion and Flame, Vol. 71, p. 313 (1988).
6. Yoshida, A. and Tsuji, H., 17th Symposium (International) on Combustion, The Combustion Institute, p. 945 (1974).
7. Yoshida, A., 18th Symposium (International) on Combustion, The Combustion Institute, p. 931 (1981).
8. Shepherd, I. G. and Moss, J. B., AIAA Journal, Vol. 20, No. 4, p. 566 (1982).
9. Cheng, R. K. and Shepherd, I. G., Combust. Sci. Tech., Vol. 52, p. 353 (1987).
10. Gulati, A. and Driscoll, J. R., Combust. Sci. Tech., Vol. 48, p. 285 (1986).
11. Gulati, A. and Driscoll, J. F., 21st Symposium (International) on Combustion, The Combustion Institute, p. 1367 (1986).
12. Driscoll, J. F. and Gulati, A., Combustion and Flame, Vol. 72, p. 131 (1988).
13. Cho, P., Law, C. K., Hertzberg, J. R. and Cheng, R. K., 21st Symposium (International) on Combustion, The Combustion Institute, p. 1493 (1986).
14. Cho, P., Law, C. K., Cheng, R. K. and Shepherd, I. G., 22nd Symposium (International) on Combustion, The Combustion Institute (1988).
15. Klimov, A. M., Progress in Astronautics and Aeronautics, Vol. 88 (J. B. Bowen et al., Ed.), AIAA, New York, p. 146 (1983).
16. Bray, K. N. C., Libby, P. A., Masuya, G. and Moss, J. B., Combust. Sci. Tech., Vol. 25, p. 127 (1981).
17. Mandelbrot, B. B., Institute of Electrical and Electronic Engineers, IEEE Transactions on Communications and Technology, COM-13, p. 77-91 (1965).
18. Kolmogorov, A. N., C.R. Academie Des Sciences de URSS, Vol. 30, p. 299 (1941).
19. Mandelbrot, B. B., Journal of Fluid Mechanics, vol. 72, p. 401-416 (1975).
20. Voss, R. F. in The Science of Fractal Images, (Peitgen, H. O., and Saupe, D. Ed., Springer-Verlag, New York, 1988, Vol. 1, p. 4).
21. Hentschel, H. G. E., and Procaccia, I., A Physical Review, Vol. 29, p. 1461-1470 (1984).
22. Procaccia, I., Journal of Statistical Physics, Vol. 5, p. 649-663 (1984).
23. Lovejoy, S., Science, Vol. 216, p. 185-187 (1982).

24. Sreenivasan, K. R., and Meneveau, C., Journal of Fluid Mechanics, Vol. 173, p. 357-386 (1986).
25. Gouldin, F. C., Combustion and Flame, Vol. 68, p. 249-266 (1987).
26. Tennekes, H., and Lumley, J. L., A First Course in Turbulence, MIT Press, Cambridge, Mass, 1972.
27. Kerstein, A. R., Combust. Sci. and Tech., (1988).
28. North, G. L., and Santavicca D. A., "Fractal Analysis of Premixed Turbulent Flame Structure," Fall Technical Meeting, ESSCI, December 1986.
29. Peters, N., 21st Symposium (International) on Combustion, The Combustion Institute, 1986, p. 1231-1250.
30. Mantzaras, J., Felton, P. G., and Bracco, F. V., Combust. and Flame, December 1987.
31. Mantzaras, J., Felton, P. G., and Bracco, F. V., SAE Paper 881635, (1988).
32. Murayama M. and Takeno, T., 22nd Symposium (International) on Combustion, The Combustion Institute, 1988, in Press.
33. Strahle, W. C. and Jagoda, J. I., 22nd Symposium (International) on Combustion, The Combustion Institute, 1988.
34. Gouldin, F. C., Hilton, S. M. and Lamb, T., 22nd Symposium (International) on Combustion, The Combustion Institute, 1988.
35. Witten, Jr., T. A. and Sander, L. M., Physical Review Letters, Vol. 47, 1400-1403 (1981).
36. Meneveau, C. and Sreenivasan, K. R., Physical Review Letters, Vol. 59, p. 1424-1427 (1987).
37. North, G. L. and Santavicca, D. A., "Fractal Analysis of Turbulence-Flame Interactions," Fall Technical Meeting, ESSCI, December 1988.
38. Schelkin, K. I., NACA TN #1110 (1947).
39. Pope, S. B. and Anand, M. S., 20th Symposium (International) on Combustion, The Combustion Institute, Pittsburgh, 1984.
40. Kilmov, A. M., Flames Lasers and Reactive Systems, Vol. 88 of Progress in Astronautics and Aeronautics, (J. R. Bowen, N. Manson, A. K. Oppenheim, and R. K. Solokhin, eds.), American Institute of Aeronautics and Astronautics, New York, p. 133-146, 1983.
41. Damkohler, G. Z., Electrochem, Vol. 46, p. 601 (1940).
42. Clavin, P. and Williams, F., Journal of Fluid Mechanics, Vol. 116, p. 251-282 (1982).
43. Mickelson, W. R. and Ernstein, N. E., 6th Symposium (International) on Combustion, The Combustion Institute, 1956.
44. Santavicca, D. A., "Turbulence Effects on Ignition Flame Kernel Growth," Invited Paper, Fall Technical Meeting, ESSCI, December 1988.
45. Abdul-Gayed, R. G., Bradley, D., Lawes, M. and Lung, F. K.-K., 21st Symposium (International) on Combustion, The Combustion Institute, 1986.

46. Pope, S. B. and Cheng, W. K., 21st Symposium (International) on Combustion, The Combustion Institute, 1986.
47. Ho, C. M., Legutko, T. L. and Santavicca, D. A., "Ignition Kernel Growth Under Idle Simulated Conditions," submitted to 1989 SAE Fuels and Lubricants Meeting.
48. Sloane, T. M. and Schoene, A. Y., 22nd Symposium (International) on Combustion, The Combustion Institute, 1988.
49. Cairns, K. D. and Santavicca, D. A., "PLIF OH Measurements in Ignition Flame Kernels," Fall Technical Meeting, ESSCI, December 1988.

### PUBLICATIONS

"Flame-Turbulence Interactions in a Freely Propagating Premixed Flame," by B. D. Videto and D. A. Santavicca, submitted to Combustion Science and Technology (April 1989).

"The Fractal Nature of Premixed Turbulent Flames," by G. L. North and D. A. Santavicca, submitted to Combustion and Flame (April 1989).

"A Fractal Model of Turbulent Flame Kernel Growth," by D. A. Santavicca, D. Liou and G. L. North, submitted to Combustion and Flame (April 1989).

### PROFESSIONAL PERSONNEL

D. A. Santavicca, Principal Investigator  
D. Liou, Ph.D. student  
G. L. North, Ph.D. student (AFRAPT Trainee)  
E. Tucker, M.S. student (AFRAPT Trainee)  
B. D. Videto, Ph.D. student  
C. A. Wilson, M. S. student (degree completed 9/88)  
J. G. Zoeckler, M. S. student (degree completed 9/88)

### INTERACTIONS

Results from this research were presented at the following meetings and seminars:

"Turbulence Effects on Ignition Flame Kernel Growth," D. A. Santavicca, Invited Paper, Fall Meeting of the ESSCI, December 1988.

"Fractal Analysis of Turbulence-Flame Interactions," G. L. North and D. A. Santavicca, 21st DHC Mtg., Ford Motor Co., October 1988 and Fall Meeting of ESSCI, December 1988.

"A Fractal Model of Turbulent Flame Kernel Growth," D. A. Santavicca, General Motors Research Laboratories, January 1989 and Wright Research and Development Center, March 1989.

The research on the turbulent flame kernel growth model has been jointly supported by this AFOSR grant and by Garrett Turbine Division. In addition to the ignition model development, an experimental study of turbulent flame kernel growth using a Garrett ignitor system is being conducted at Penn State in close collaboration with Garrett personnel.